Mitochondrial DNA replication stress triggers a pro-inflammatory endosomal pathway of nucleoid disposal

A list of authors and their affiliations appears at the end of the paper

Mitochondrial DNA (mtDNA) encodes essential subunits of the oxidative phosphorylation system, but is also a major damage-associated molecular pattern (DAMP) that engages innate immune sensors when released into the cytoplasm, outside of cells or into circulation. As a DAMP, mtDNA not only contributes to anti-viral resistance, but also causes pathogenic inflammation in many disease contexts. Cells experiencing mtDNA stress caused by depletion of the mtDNA-packaging protein, transcription factor A, mitochondrial (TFAM) or during herpes simplex virus-1 infection exhibit elongated mitochondria, enlargement of nucleoids (mtDNA–protein complexes) and activation of cGAS–STING innate immune signalling via mtDNA released into the cytoplasm. However, the relationship among aberrant mitochondria and nucleoid dynamics, mtDNA release and cGAS–STING activation remains unclear. Here we show that, under a variety of mtDNA replication stress conditions and during herpes simplex virus-1 infection, enlarged nucleoids that remain bound to TFAM exit mitochondria. Enlarged nucleoids arise from mtDNA experiencing replication stress, which causes nucleoid clustering via a block in mitochondrial fission at a stage when endoplasmic reticulum actin polymerization would normally commence, defining a fission checkpoint that ensures mtDNA has completed replication and is competent for segregation into daughter mitochondria. Chronic engagement of this checkpoint results in enlarged nucleoids trafficking into early and then late endosomes for disposal. Endosomal rupture during transit through this endosomal pathway ultimately causes mtDNA-mediated cGAS–STING activation. Thus, we propose that replication-incompetent nucleoids are selectively eliminated by an adaptive mitochondria–endosomal quality control pathway that is prone to innate immune system activation, which might represent a therapeutic target to prevent mtDNA-mediated inflammation during viral infection and other pathogenic states.

Improper replication, repair, or packaging of mitochondrial DNA (mtDNA) causes activation of cellular stress pathways that are only beginning to be unravelled[1–3]. For example, we showed previously that mtDNA stress caused by partial depletion or haploinsufficiency (*Tfam*^{+/−}) of transcription factor A, mitochondrial (TFAM), an abundant mtDNA-binding protein essential for transcription-primed mtDNA replication, nucleoid formation and mtDNA segregation during mitochondrial fission[4–6], results in enlarged nucleoids, elongated mitochondria

and the release of mtDNA into the cytoplasm that activates the cGAS–STING innate immune signalling pathway[7]. This response leads to the expression of interferon-stimulated genes (ISGs) that prime anti-viral immunity in cells and mice and, interestingly, also enhance nuclear DNA repair capacity[7,8]. In this Article, we endeavoured to determine the mechanism underlying how altered mitochondrial dynamics and mtDNA stress cause mtDNA release and innate immune signalling.

Results

mtDNA stress causes enlarged nucleoids to exit mitochondria

To determine the nature of the cytoplasmic mtDNA released in the context of mtDNA stress, we performed fluorescence in situ hybridization (FISH) in human primary lung fibroblasts (IMR-90) depleted of TFAM, taking advantage of previously characterized probes that target multiple regions of human mtDNA[9] (Fig. 1b). Airyscan imaging of these cells revealed that a subset of enlarged nucleoids is localized outside of mitochondria (Fig. 1a, quantified in 1c). Furthermore, immunofluorescence performed after mtDNA FISH demonstrated that cGAS is localized with these now extra-mitochondrial, enlarged nucleoids (Fig. 1a, quantified in 1d). Also, although the TFAM signal was weak and often difficult to detect in IMR-90 cells transfected with TFAM small interfering RNA (siRNA), we consistently observed TFAM colocalization with released nucleoids and cGAS (Extended Data Fig. 1a,b). Enlarged nucleoids also arise during infection by several viruses[7,10], including herpes simplex virus-1 (HSV-1), and expression of the virus-encoded HSV-1 UL12.5 nuclease causes enlarged nucleoids and mtDNA release that primes anti-viral responses, before it eventually depletes mtDNA[7,11,12]. When expressed in U2OS cells, UL12.5 depleted mtDNA and reduced TFAM levels as previously shown[7], and also caused the release of enlarged nucleoids that colocalized with cGAS and TFAM (Extended Data Fig. 1c–f). These results prompted us to examine whether the release of whole nucleoids occurs during an actual HSV-1 infection. We previously demonstrated that HSV-1 induces enlarged nucleoids 6 h after infection (with subtle changes in nucleoid morphology beginning at 3 h), ultimately leading to mtDNA depletion 12 h after infection[7]. We therefore imaged TFAM as a marker for extra-mitochondrial nucleoids in cells fixed 4, 6, 8 and 10 h after HSV-1 infection. Remarkably, we observed enlarged nucleoids localized outside of mitochondria, peaking 8 h after infection (Fig. 1e,f) and corroborating our results with TFAM depletion and UL12.5 expression. Altogether, these results demonstrate that nucleoids are released under multiple mtDNA stress conditions, including HSV-1 infection, and that these remain bound to TFAM. These results are consistent with longer DNA molecules that are bound and extensively bent by TFAM being endogenous substrates for cGAS binding and activation[13].

Enlarged nucleoids are not released through BAX/BAK or VDAC pores

We next asked how enlarged nucleoids escape from mitochondria. One mechanism for the removal/release of entire mtDNA nucleoids that also activates cGAS–STING signalling is through large BAK/BAX pores under conditions of caspase-inhibited apoptosis[14,15]. However, this does not appear to be occurring with TFAM deficiency in either murine embryonic fibroblasts (MEFs) or in U2OS cells (generated by clustered regularly interspaced short palindromic repeats (CRISPR), Extended Data Fig. 2), as we were unable to detect the presence of BAX pores in $Tfam^{+/-}$ MEFs (Extended Data Fig. 3a,b), did not observe any obvious inner-membrane herniation around enlarged nucleoids in TFAM-depleted U2OS cells (Extended Data Fig. 3c) and still observed extra-mitochondrial nucleoids in TFAM-depleted $Bak^{-/-}Bax^{-/-}$ MEFs (Extended Data Fig. 3d,e). Another mechanism involves the release of mtDNA fragments through pores composed of VDAC1 or VDAC3 oligomers[16]. Although this mechanism does not explain the release of entire nucleoids, we nonetheless decided to test for the role of VDAC pores under mtDNA stress conditions, in case shorter mtDNA fragments were also being released and driving cGAS–STING signalling. Depletion of VDAC1 or VDAC3 had no effect on ISGs in $Tfam^{+/-}$ MEFs (Extended Data Fig. 4a–d). In addition, pharmacological inhibition of VDACs using VBIT4 did not affect the number of extra-mitochondrial nucleoids or colocalization with cGAS in UL12.5-expressing cells (Extended Data Fig. 4e,f), supporting the conclusion that enlarged nucleoids, and not mtDNA fragments, are released to activate cGAS within this context of mtDNA stress.

Enlarged nucleoids escape mitochondria via membrane compartments

Since previously known mtDNA release mechanisms were apparently not at play, we next endeavoured to capture the mtDNA release events by correlative light and electron microscopy (CLEM). Live TFAM-deficient U2OS cells labelled with the DNA intercalating dye Pico-Green, cGAS–mCherry, TOM20–Halo and mTurquoise–LC3 (for fiducial information) were imaged using Airyscan microscopy until an apparent mtDNA-extrusion event in progress was observed, at which point the cell was immediately fixed on the microscope stage (Fig. 2a). The same cell was then located and imaged using serial section scanning electron microscopy (SEM), after which the CLEM datasets were aligned (Fig. 2b). We identified a corresponding structure positive for PicoGreen and cGAS–mCherry, but negative for TOM20–Halo and mTurquoise–LC3, that was emerging from a TOM20-positive mitochondrion (Fig. 2c,d), with the SEM data indicating that enlarged nucleoids can be extruded from mitochondria within a membrane-bound compartment. Unlike previously described inner mitochondrial membrane herniations[14,15], these compartments did not appear to be extruding through a break in the outer mitochondrial membrane. Mitochondria-derived vesicles (MDVs) can bud from mitochondria and carry mitochondrial cargo to the lysosome, and recently these were reported to carry mtDNA as cargo within the context of fumarate hydratase deficiency[17,18]. However, the PicoGreen- and cGAS–mCherry-positive structures that we observed are much larger than inner mitochondrial membrane-derived MDVs,
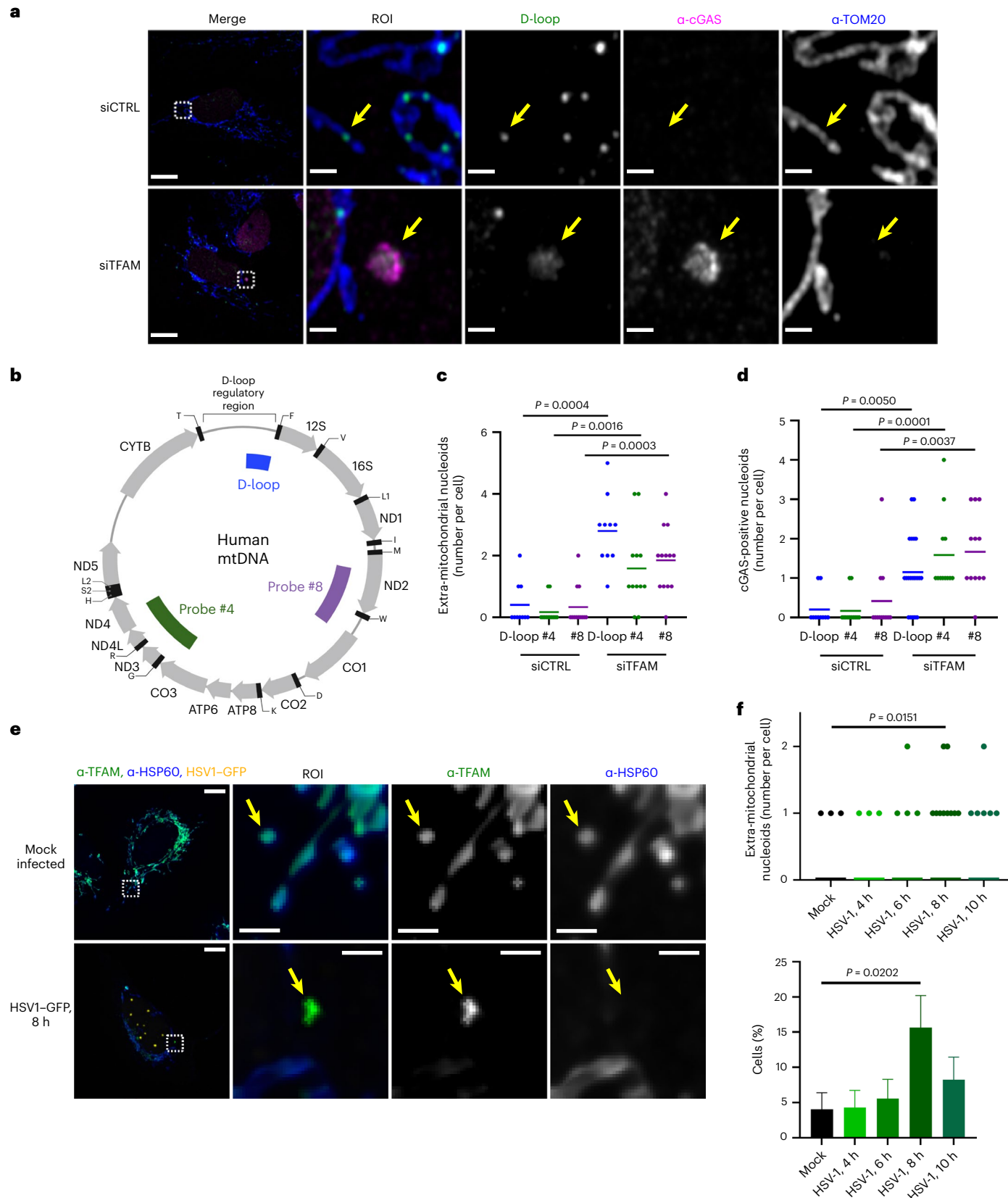
**Fig. 1 | mtDNA stress results in TFAM-bound, extra-mitochondrial nucleoids. a**, Airyscan imaging of mtDNA FISH (D-loop probe), followed by immunofluorescence against cGAS and TOM20 in IMR-90 cells transfected with control or TFAM siRNAs. Scale bars, 10 μm and inset scale bars, 1 μm. **b**, A schematic showing the regions of human mtDNA complementary to the three FISH probes used: D-loop, probe #4 (ND2–COI) or probe #8 (COII–ND4)[9,46]. **c**, Quantification of extra-mitochondrial mtDNA. siCTRL (control) and siTFAM were compared ($P = 0.0004$ for D-loop, $P = 0.0016$ for probe #4 and $P = 0.0003$ for probe #8). For the D-loop probe, $N = 10$ cells for siCTRL and siTFAM; for probe #4, $N = 12$ cells for siCTRL and siTFAM; for probe #8, siCTRL $N = 12$ cells and siTFAM N = 13 cells. Data were quantified from one representative experiment of three. **d**, Overlap of extra-mitochondrial mtDNA with cGAS. siCTRL and siTFAM were compared ($P = 0.005$ for D-loop, $P = 0.0001$ for probe #4 and $P = 0.0037$ for probe #8). For the D-loop probe, siCTRL $N = 10$ cells and siTFAM $N = 20$ cells; for both probe #4 and probe #8, $N = 12$ cells for siCTRL and siTFAM.

Data were quantified from one representative experiment of three. **e**, Spinning disk imaging of TFAM and HSP60 immunofluorescence in a U2OS cell 8 h after infection with HSV-1–GFP. The image display settings of TFAM are not constant between conditions, to account for diminished TFAM levels caused by HSV-1 infection[7]. Larger scale bar, 10 μm and inset scale bars, 2 μm. **f**, Quantification of non-mitochondrial TFAM at the indicated timepoints after infection. Mock and infected cells were compared ($P = 0.0151$ for the number of extra-mitochondrial nucleoids and $P = 0.0202$ for the percentage of cells with extra-mitochondrial nucleoids). Number of cells: $N = 70$ for mock, $N = 71$ for 4 h, $N = 74$ for 6 h, $N = 64$ for 8 h and $N = 73$ for 10 h. Data were pooled from three independent experiments. The same dataset was used to generate both graphs shown in **f**. The bottom graph shows the percentage of cells with extra-mitochondrial mtDNA, and data are presented as mean ± s.e.m. All differences were compared using an unpaired, two-tailed Student's t-test. For all images, lines represent the mean. Source numerical data are available in Source data.

which are ~100 nm in diameter[17,19]. Furthermore, mtDNA-containing MDVs have thus far only been described to carry normal-sized nucleoids, as opposed to enlarged nucleoids[18]. Finally, mtDNA-positive MDVs arising from fumarate hydratase deficiency do not colocalize with cGAS[18], again differentiating them from the mtDNA-containing structures that we observe. Therefore, we conclude that enlarged,

stressed nucleoids exit mitochondria through previously uncharacterized membrane-bound compartments.

We next performed CLEM experiments using HSV-1 UL12.5 expression as an alternative method to induce mtDNA stress and release. For these experiments, we imaged cells after fixation, using TFAM–green fluorescent protein (GFP) as a marker for extra-mitochondrial


Fig. (a) Merge, ROI, D-loop, α-cGAS, α-TOM20 panels for siCTRL and siTFAM. (b) Human mtDNA map showing D-loop regulatory region, D-loop, Probe #4, Probe #8. (c) Extra-mitochondrial nucleoids (number per cell). (d) cGAS-positive nucleoids (number per cell). (e) α-TFAM, α-HSP60, HSV1–GFP panels for Mock infected and HSV1–GFP, 8 h. (f) Extra-mitochondrial nucleoids and Cells (%).
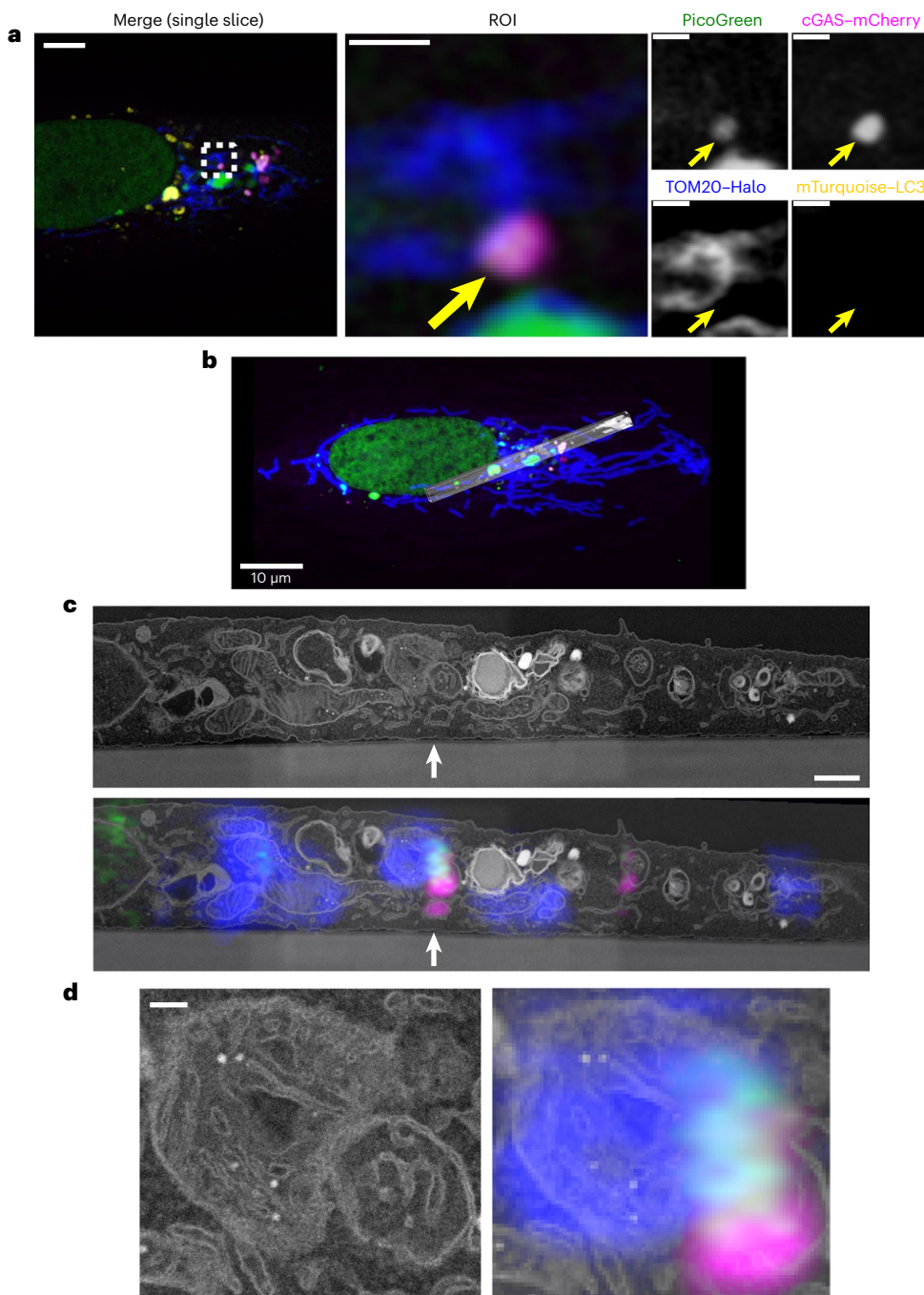
Fig. 2 | Defective nucleoids escape from mitochondria in membrane compartments. a–d, TFAM-deficient U2OS cells (TF^D-1) were imaged live using Airyscan microscopy until a cGAS-positive nucleoid was observed to be exiting mitochondria. The cell was fixed on the microscope stage and processed for CLEM (Methods). A total of ten cells were imaged live and fixed (one cell per gridded coverslip), and one cell was selected for full CLEM analysis. **a**, Airyscan imaging of a TFAM-deficient cell immediately after fixation. One *z* slice is shown. Arrows highlight a nucleoid leaving mitochondria. Scale bar, 5 μm and inset scale bars, 1 μm. **b**, Following fixation, the cell was processed for serial section 3D SEM. An overview of the entire cell shows SEM data sections aligned to fluorescence data (*z*-stack projection). **c**, One SEM slice, alone (top) or aligned to fluorescence data (bottom image) is shown. The arrowhead indicates mtDNA exiting mitochondria as shown in **a**. Scale bar, 1 μm. **d**, Enlargement of ROI from aligned CLEM data (right) and only EM data (left). Scale bar, 200 nm.

mtDNA. We characterized three instances of TFAM–GFP that were colocalized with cGAS–mCherry, but not TOM20–Halo. Notably, these structures did not colocalize with mTurquoise–LC3 (Fig. 3a). After imaging this cell by focused ion beam microscopy (FIB–SEM) and aligning the CLEM datasets, we observed that all three regions of interest (ROIs) corresponded with membrane-bound compartments. FIB–SEM imaging of these is shown in Fig. 3b, and three-dimensional (3D) rendering of these structures (for visualization) is shown in Fig. 3c (Supplementary Videos 1 and 2). On the basis of these results,

we propose that the nucleoid trafficking pathway that we have uncovered occurs in response to multiple forms of mtDNA stress and is not an idiosyncratic response to genetic TFAM depletion.

Enlarged nucleoids traffic through the endosomal pathway for disposal after exiting mitochondria

A clue to the nature of these mtDNA-containing vesicular compartments came from parallel, cryo-electron tomography experiments in *Tfam*$^{+/-}$ MEFs, in which we consistently observed multi-membrane
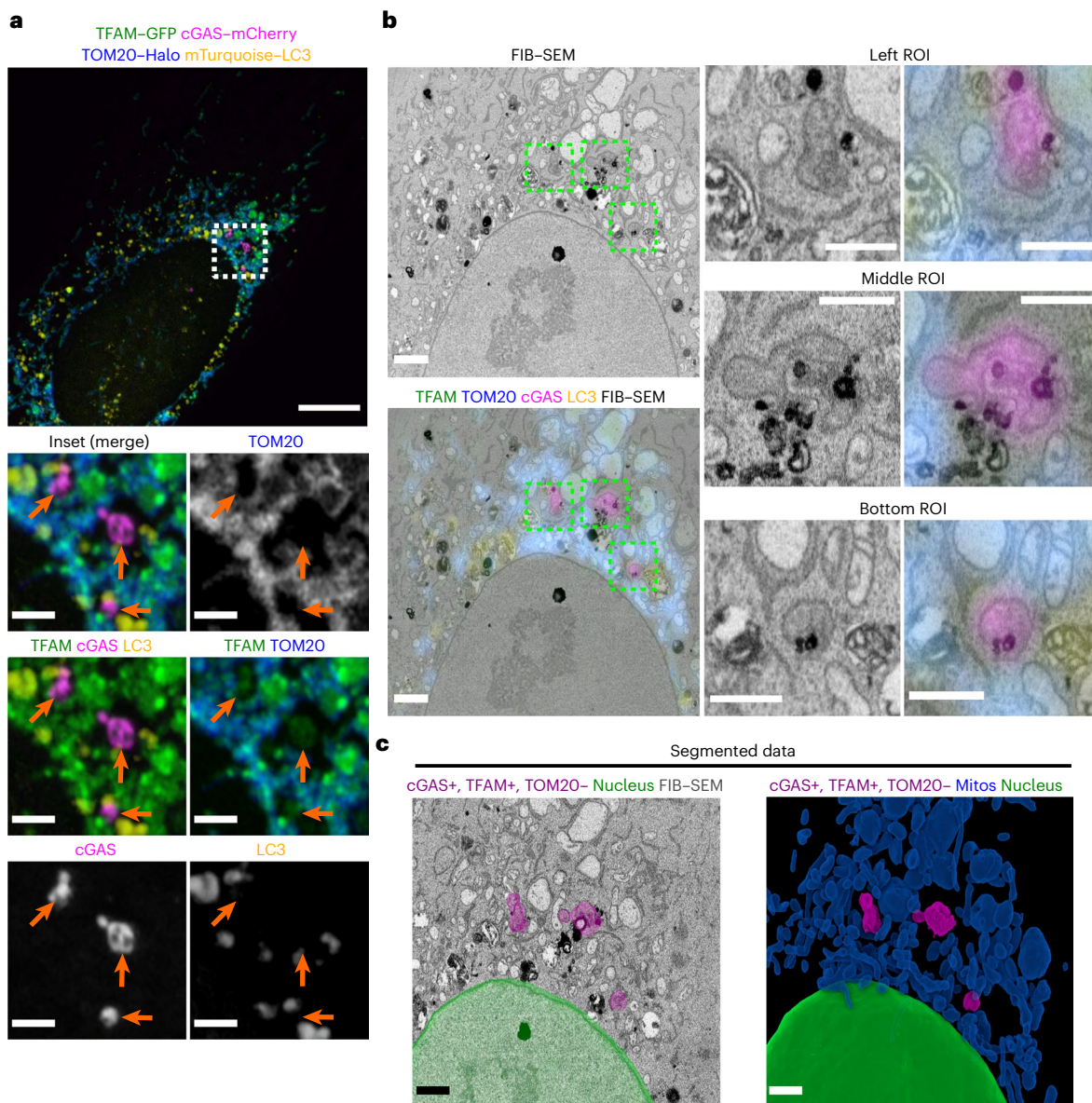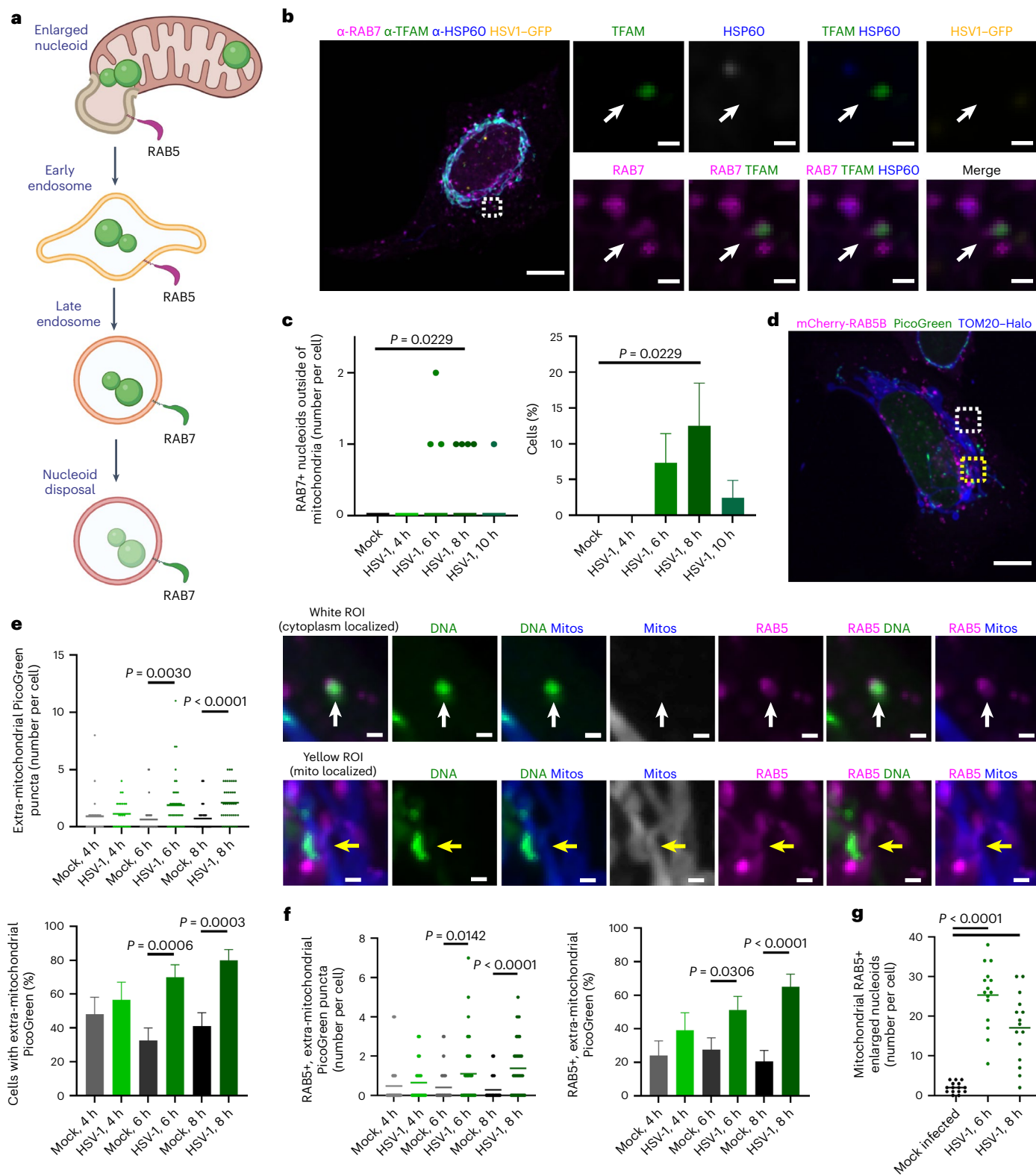
Fig. 3 | HSV-1 UL12.5 triggers membrane trafficking of nucleoids. a–c, CLEM of a U2OS cell expressing HSV-1 UL12.5. Cells were imaged post-fixation, and TFAM–GFP was used as a marker for mtDNA. A total of 12 cells were imaged across two gridded coverslips, and one cell was selected for full CLEM analysis. **a,** Airyscan imaging of a cell that was selected for CLEM. Arrows highlight three non-mitochondrial TFAM–GFP puncta overlapping with cGAS–mCherry, but not mTurquoise–LC3. Scale bar, 10 μm and inset scale bars, 1 μm. **b,** The cell from **a** was imaged by FIB–SEM, and the EM (top) and CLEM (bottom) data are shown. The insets highlight both EM (left) and CLEM (right) data of three

TFAM/cGAS puncta (green boxes) identified from **a** (arrows). Scale bars, 2 μm and inset scale bars, 1 μm. **c,** Three-dimensional rendering of FIB–SEM data from the cell shown in **b.** TFAM + , cGAS+ structures (purple) as well as the nucleus (green) were segmented and overlaid onto the FIB–SEM data (top). The bottom image shows segmentation and 3D rendering of TFAM+, cGAS+ structures (purple), mitochondria (Mitos; blue) and the nucleus (green). Scale bars, 2 μm. This experiment was performed once (the observation of nucleoids present in membrane compartments was reproduced in Fig. 2).

structures that resembled multi-vesicular bodies (MVBS; Extended Data Fig. 5a,b), which are a type of late endosome[20]. A representative cryo-electron tomogram slice is shown (Extended Data Fig. 5a), and these data were reconstructed and segmented for better visualization (Extended Data Figs. 5b and 6). Therefore, we hypothesized that *Tfam*^{+/−} MEFs are experiencing increased flux through the endosomal system, and we decided to repeat mtDNA FISH experiments in combination with immunofluorescence to visualize the late endosomal marker RAB7. We observed RAB7 overlapping with cGAS-positive nucleoids located outside mitochondria in TFAM-depleted cells (Extended Data Fig. 5c,g), as well as RAB7A–GFP overlapping with both cytoplasmic TFAM and cGAS–mCherry in U2OS cells expressing HSV-1 UL12.5 (Extended Data

Fig. 5d,h). These results demonstrate that enlarged, released nucleoids eventually traffic through RAB7-positive structures. To determine whether mtDNA was present within endolysosomes, we tested whether these compartments were able to acidify. In live cells expressing UL12.5, we observed that a subset of extra-mitochondrial PicoGreen puncta were also positive for LysoTracker Deep Red, which labels acidified compartments (Extended Data Fig. 5e,f,i,j). Therefore, we propose that trafficking of enlarged nucleoids into late endosomes mediates their ultimate disposal within lysosomes.

We next asked how enlarged nucleoids might arrive at RAB7-marked compartments. One possibility is that mitochondria containing enlarged nucleoids could be targeted for degradation by mitophagy.

RAB7 also marks lysosomes, which fuse to autophagosomes during the final steps of autophagy, and this mechanism could explain how mtDNA might colocalize with RAB7 as a result of mitophagy. While the lack of colocalization of LC3 with extra-mitochondrial enlarged nucleoids (Figs. 2 and 3) suggested that this is not the case, we nevertheless decided to measure mitophagy rates under conditions of mtDNA release, and we found that mitophagic flux in cells expressing HSV-1 UL12.5 was similar to control cells (Extended Data Fig. 5k). Therefore, we

sought another explanation for how mtDNA arrives in RAB7 compartments. Early endosomes receive endocytosed cargo from the plasma membrane, mediated by RAB5, and sort cargo into late endosomes in a RAB7-dependent manner[21]. We therefore hypothesized that this pathway might similarly receive cargo from mitochondrial membranes to facilitate the degradation of the offending nucleoids via trafficking through both early and late endosomes. In support of this idea, it has been reported that early endosomes can engulf mitochondria

Fig. 4 | HSV-1 infection triggers endosomal trafficking of nucleoids. a, Model of endosomal disposal of enlarged nucleoids from mitochondria. **b**, Spinning disk imaging of RAB7, TFAM and HSP60 immunofluorescence in a U2OS cell 8 h after infection with HSV-1–GFP. Larger scale bar, 10 μm and inset scale bars, 1 μm. **c**, The number of non-mitochondrial TFAM puncta overlapped with RAB7 was scored. Mock and infected cells were compared ($P = 0.0229$). Number of cells: $N = 39$ cells for mock, $N = 37$ for 4 h, $N = 41$ for 6 h, $N = 32$ for 8 h and $N = 41$ for 10 h. Data were pooled from three independent experiments. The same dataset was used to generate both graphs. **d**, Spinning disk imaging of mCherry–RAB5B, PicoGreen and TOM20–Halo in live cells 7 h after infection with HSV-1–mCerulean. The brightness of the top ROI DNA signal is saturated for easier visualization. Larger scale bar, 10 μm and inset scale bars, 1 μm. **e**, The number of extra-mitochondrial PicoGreen puncta was scored. Mock and infected cells were compared (number of nucleoids: $P = 0.003$ for 6 h and $P < 0.0001$ for 8 h; percentage of cells:

$P = 0.0006$ for 6 h and $P = 0.0003$ for 8 h). **f**, The number of extra-mitochondrial PicoGreen puncta overlapped with RAB5 was scored. Mock and infected cells were compared (number of nucleoids: $P = 0.0142$ for 6 h and $P < 0.0001$ for 8 h; percentage of cells: $P = 0.0306$ for 6 h and $P < 0.0001$ for 8 h). N (number of cells) for all graphs in **e** and **f**: mock 4 h, $N = 25$; HSV-1 4 h, $N = 23$; mock 6 h, $N = 40$; HSV-1 6 h, $N = 39$; mock 8 h, $N = 39$; and HSV-1 8 h, $N = 40$. The experiment was performed three times, and data were pooled from two independent experiments. The same dataset was used to generate all graphs in **e** and **f**. **g**, Mitochondria-localized enlarged nucleoids were identified on the basis of size (>0.36 μm^2) and scored for the presence of mCherry–RAB5B. Mock and infected cells were compared ($P < 0.0001$). $N = 15$ cells per condition. Data were quantified from one of three representative experiments. All differences were compared using an unpaired, two-tailed Student's t-test. In all graphs, lines represent the mean, error bars represent s.e.m. Source numerical data are available in Source data.
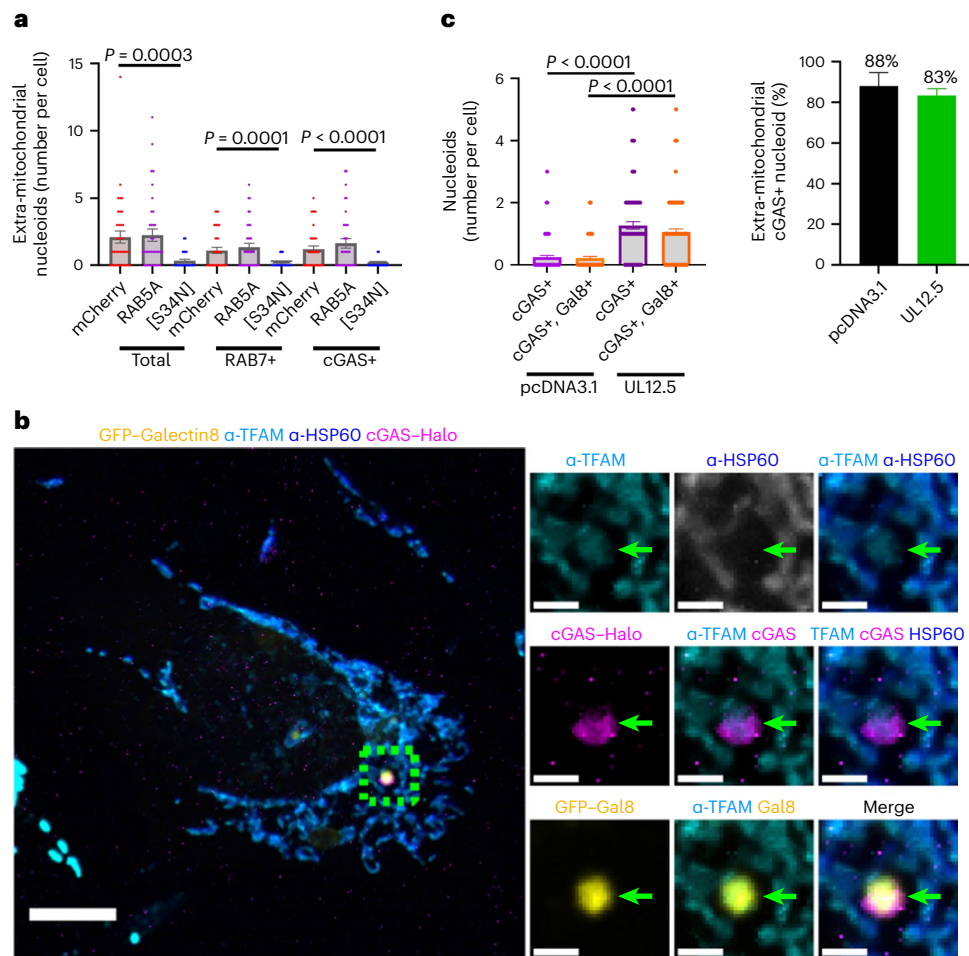

Fig. 5 | Rupture of late endosomes leads to access of cGAS to mtDNA that is trafficking through the endosomal pathway. a, Quantification of extra-mitochondrial TFAM immunofluorescence and colocalization with either RAB7 immunofluorescence or cGAS–Halo, in U2OS cells expressing HSV-1 UL12.5 and either mCherry, mCherry–RAB5A or mCherry–RAB5A[S34N]. mCherry and RAB5[S34N] expressing cells were compared ($P = 0.0003$ for total extra-mitochondrial nucleoids, $P = 0.0001$ for RAB7+ nucleoids and $P < 0.0001$ for cGAS+ nucleoids). $N = 35$ cells for each condition. The experiment was performed three times, and data were pooled from two independent experiments. **b**, Spinning disk imaging of TFAM and HSP60 immunofluorescence in a U2OS cell expressing cGAS–Halo and GFP–Gal8. Larger scale bar, 10 μm and inset scale

bars, 2 μm. **c**, Left: extra-mitochondrial TFAM puncta that were positive for cGAS were also scored for the presence of Gal8 (Gal8+). pcDNA3.1 and UL12.5 transfected cells were compared ($P < 0.0001$). $N = 100$ cells for pcDNA3.1 and $N = 99$ cells for UL12.5. Data were pooled from three independent experiments. Right: the percentage of extra-mitochondrial, cGAS-positive nucleoids that were also positive for Gal8 is plotted. $N = 25$ nucleoids for pcDNA3.1 and $N = 126$ nucleoids for UL12.5. The same dataset was used to generate both graphs in **c**. All differences were compared using an unpaired, two-tailed Student's t-test. For all graphs, data are represented as mean ± s.e.m. Source numerical data are available in Source data.

to mediate mitochondrial clearance[22], that the retromer complex can extract normal-sized nucleoids and deliver them to endosomes for endolysosomal-mediated disposal[23], and that endosome–mitochondria contacts resulting from disrupted mitochondrial fusion can

promote relocalization of mtDNA to endosomes, where TLR9 activation and signalling occurs[24]. To assay the potential colocalization of enlarged nucleoids with RAB5, we imaged live cells instead of fixed cells, because we found that RAB5-labelled structures are poorly preserved

in fixed samples. We observed that enlarged nucleoids colocalized with mCherry–RAB5 when present outside of mitochondria (Extended Data Fig. 5l,m) in UL12.5-expressing cells, indicating that enlarged nucleoids traffic into early endosomes in addition to late endosomes, and further implicating a canonical endosomal pathway in the trafficking of released, defective mtDNA.

From these above results, we hypothesized that enlarged nucleoids are trafficked into early endosomes, which mature into late endosomes and ultimately lysosomes for disposal (Fig. 4a). To test this model and establish the kinetics of enlarged nucleoids trafficking through this pathway, we used the HSV-1 infection model. We observed that extra-mitochondrial TFAM colocalized with RAB7, and that the appearance of released TFAM/RAB7 puncta peaked 8 h after infection, following similar kinetics (Fig. 4b,c) as total released TFAM (Fig. 1e,f). We did not observe colocalization of released TFAM with LC3 (Extended Data Fig. 7a,b) during HSV-1 infection, despite of the fact that we were able to measure an increase in LC3 puncta intensity over the time course we examined (Extended Data Fig. 7c–e), supporting our conclusion that mitophagy is not mediating the removal of enlarged nucleoids. To continue establishing the kinetics of mtDNA trafficking along the endosomal pathway, we next assayed for colocalization of cytosolic DNA with the early endosomal marker mCherry–RAB5 after HSV-1 infection. We performed these experiments in live cells, again due to RAB5 signals being poorly preserved after cellular fixation. We also used PicoGreen to label mtDNA, as we found that overexpression of a fluorescently tagged TFAM protected against mtDNA release caused by HSV-1, which incidentally is consistent with depletion of TFAM triggering mtDNA release[7]. We observed an early increase in non-mitochondrial PicoGreen colocalized with mCherry–RAB5 (Fig. 4d–f; omitting the 10 h timepoint that was confounded by imaging of replicated HSV-1 DNA). Nucleoids in early endosomal (RAB5+) compartments arose earlier (6 h post-infection) than those in late endosomal (RAB7+) compartments (8 h post-infection) (Fig. 4b,c), consistent with our model (Fig. 4a) and corroborating our earlier observations that UL12.5 causes relocalization of nucleoids into RAB5+ structures (Extended Data Fig. 5l,m). Collectively, these results support a model in which defective nucleoids exit mitochondria and are then trafficked through the endosomal pathway for ultimate degradation (Fig. 4a).

Endosomal rupture enables mtDNA release and access to cGAS
We next turned to the question of how the relocalization of nucleoids to endosomal compartments enables cGAS activation. RAB5 is recruited to the outer mitochondrial membrane in several contexts[25–27]. Remarkably, we consistently observed colocalization of mCherry–RAB5 with mitochondria-localized enlarged nucleoids (Fig. 4d,g) at the same timepoints when nucleoids were exiting mitochondria (Fig. 4d–f). Therefore, we co-expressed UL12.5 in conjunction with a dominant-negative mutant of RAB5, to block RAB5 activation. Inhibiting RAB5 activity not only reduced the colocalization of nucleoids with RAB7, but also their colocalization with cGAS, and resulted in an overall reduction in the total amount of extra-mitochondrial mtDNA (Fig. 5a). These data indicate that RAB5 activity is required for nucleoid trafficking

to late endosomes and ultimate colocalization with cGAS. Having established that RAB5 activation ultimately facilitates the colocalization of enlarged nucleoids with cGAS, we next addressed how cGAS (an enzyme that binds cytosolic and nuclear DNA) could recognize mtDNA confined within endosomal compartments. One possibility is that late endosomes can rupture if they are unable to fully mature into lysosomes[28]. Therefore, we assayed for colocalization of cGAS-positive mtDNA with galectin 8 (Gal8), a marker of ruptured endosomes[28]. We found that a high percentage (>80%) of cGAS-marked mtDNA colocalized with Gal8 (Fig. 5b,c), indicating that endosomal rupture enables cGAS access to mtDNA trafficking through the endosomal pathway.

Failed mtDNA replication stalls mitochondrial fission, resulting in enlarged nucleoids that traffic through the endosomal pathway
On the basis of the results above, we propose that the endosomal pathway mediates the disposal of enlarged, defective nucleoids, and that the failure of this pathway to efficiently traffic excessive released nucleoids causes cGAS–STING signalling via ruptured endosomes. However, the precise nature of the mtDNA defect that instigates mtDNA disposal leading to its release, and whether this is linked to mitochondrial elongation observed under these conditions, remained unclear. To address this, we next tried to determine the replication status of the enlarged nucleoids in TFAM-depleted MEFs by measuring their rate of 5-ethynyl-2′-deoxyuridine (EdU) incorporation. The rate of EdU incorporation within enlarged nucleoids was reduced compared with their smaller, more typical counterparts in the same cells within a short (4 h) pulse (Fig. 6a–e) (longer, 24 h incubation times did enable EdU incorporation into enlarged nucleoids). The diminished EdU signal in TFAM-depleted cells was not simply caused by lower overall mtDNA levels, as EdU intensity was diminished specifically within enlarged nucleoids, when compared with normal-sized nucleoids, within TFAM-depleted cells (Fig. 6c–e). To determine whether enlarged nucleoids localize to sites of mtDNA replication, we performed immunofluorescence against components of the mtDNA replisome, and observed that Twinkle, mtSSB and POLG2 all colocalized with enlarged nucleoids (Fig. 6f). These results suggest that enlarged nucleoids comprise mtDNA molecules associated with reduced replication activity. The endoplasmic reticulum (ER) licences mtDNA replication at mitochondria–ER contact sites[29]. To determine whether the ER is present near enlarged nucleoids, we performed live cell imaging using PicoGreen in conjunction with markers of the ER (Ii33–mCherry) and mitochondria (mtBFP). Time-lapse imaging shows that the ER wraps around those enlarged nucleoids that remain inside mitochondria in both TFAM-deficient U2OS cells and U2OS cells expressing UL12.5 (Extended Data Fig. 8a–d), consistent with enlarged nucleoids arising at mtDNA replication sites and prolonged engagement of ER at these sites of mtDNA replication stress.
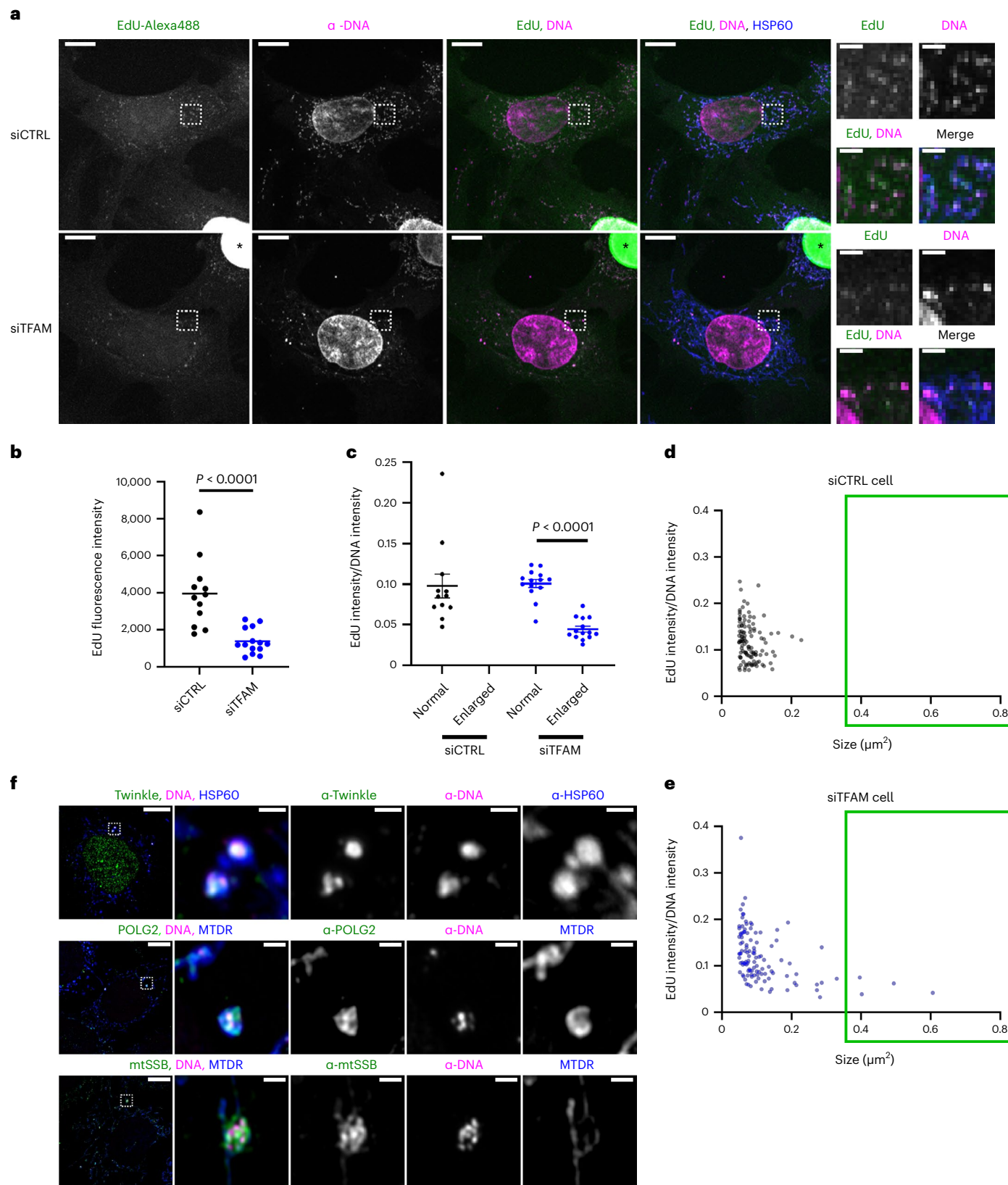
Since mitochondrial fission is tightly coupled to mtDNA replication and segregation at mitochondria–ER contact sites[29], we hypothesized that a loss of the normal coordination of mtDNA replication and fission underlies the formation and eventual exit of enlarged,

---

Fig. 6 | Enlarged nucleoids are associated with incomplete mtDNA replication. a, Pulse EdU labelling (4 h) of immortalized wild-type MEFs that were previously transfected with control or TFAM siRNAs for 96 h. *EdU incorporation within the nuclei of some cells in the population, shown as an internal positive control. Confocal images of EdU–Alexa488, DNA and HSP60 are shown. Scale bars, 10 μm for larger images and 2 μm for insets. **b**, Quantification of EdU labelling. A mask of nucleoids was created by thresholding non-nuclear DNA, and EdU fluorescence intensity was measured within the mask. siCTRL and siTFAM were compared using an unpaired, two-tailed Student's *t*-test (*P* < 0.0001). **c**, The ratio of EdU fluorescence intensity to total DNA intensity within nucleoids was measured, and nucleoids were sorted by size (enlarged are >0.4 μm²). Normal and enlarged nucleoids in siTFAM cells were compared using a paired,

two-tailed Student's *t*-test (*P* < 0.0001) (no enlarged nucleoids were observed in siCTRL cells). In **b** and **c**, *N* = 12 cells for siCTRL and *N* = 14 cells for siTFAM. Data were quantified from one representative experiment of three. **d**, The ratio of EdU intensity to total DNA intensity is plotted as a function of nucleoid size. The green box highlights area of graph corresponding to enlarged nucleoids. Data from one representative siCTRL cell is shown. **e**, The same as **d**, but data for one representative siTFAM cell is shown. **f**, Airyscan imaging of immunofluorescence against Twinkle, POLG2 or mtSSB alongside DNA in immortalized *Tfam*^{+/−} MEFs. Mitochondria were labelled using either HSP60 or Mitotracker Deep Red (MTDR). Scale bars, 10 μm for larger images and 1 μm for insets. The results are representative of three independent experiments. Data are represented as mean ± s.e.m. Source numerical data are available in Source data.

dysfunctional nucleoids. In support of this, depletion of DRP1, which mediates the final steps of mitochondrial fission[30–32], was previously shown to cause enlarged, 'clustered' nucleoids[33]. We confirmed this (Extended Data Fig. 8e–g) and also found that these enlarged nucleoids were released and colocalized with both cGAS and RAB7 (Fig. 7a,b) and led to increased expression of ISGs (Fig. 7c and Extended

Data Fig. 8h) in wild-type cells, robustly phenocopying the depletion of TFAM and expression of UL12.5. These results prompted us to examine where mitochondrial fission is stalled as a result of the replication stress occurring in TFAM-depleted cells. After ER association with mitochondria, actin polymerization on both mitochondria and ER are required for mitochondrial fission to proceed[34–39], with
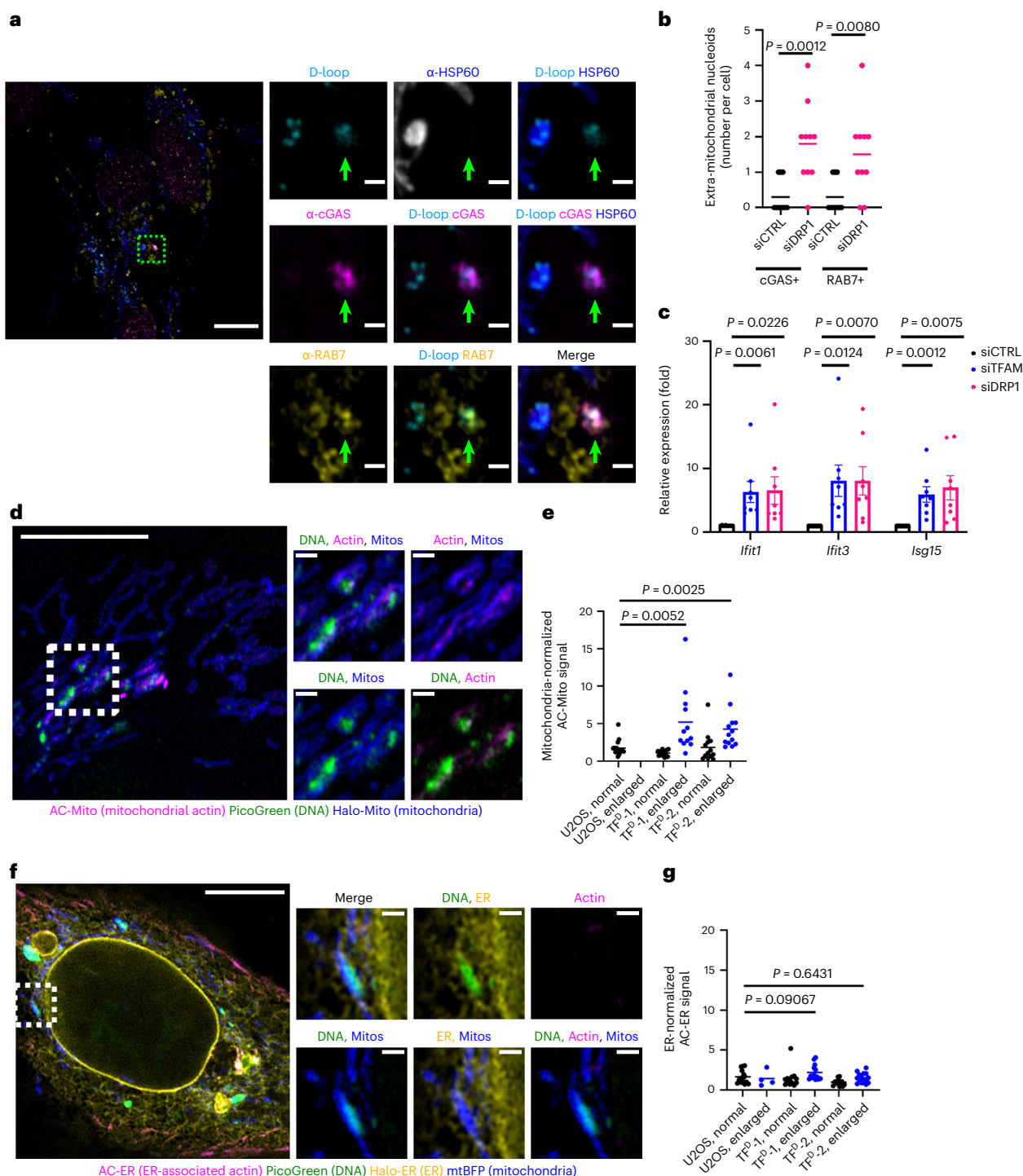
Fig. 7 | A mitochondrial fission checkpoint that ensures mtDNA replication is complete and daughter molecules are competent for segregation.
a, Airyscan imaging of mtDNA (D-loop probe), RAB7, cGAS and HSP60 in a DRP1-depleted IMR-90 cell. Scale bars, 10 μm and inset scale bars, 1 μm.
b, Quantification of **a**. $P = 0.0012$ for cGAS+ nucleoids and $P = 0.0080$ for RAB7+ nucleoids. $N = 10$ cells for each condition. **c**, Reverse transcriptase quantitative PCR of ISGs (normalized to β actin) in primary wild-type MEFs receiving control, TFAM or DRP1 siRNAs. siCTRL and siTFAM or siDRP1 were compared (siTFAM: $P = 0.0061$ for *Ifit1*, $P = 0.0123$ for *Ifit3* and $P = 0.0012$ for *Isg15*; siDRP1: $P = 0.0226$ for *Ifit1*, $P = 0.007$ for *Ifit3* and $P = 0.0075$ for *Isg15*). Eight biological replicates are represented as mean ± s.e.m. **d**, Airyscan imaging of a live TFAM-deficient U2OS cell (TF^D-1) expressing a mitochondria-targeted actin nanobody to label mitochondrial actin accumulation (AC-Mito). Scale bars, 10 μm and inset scale bars, 1 μm. **e**, Quantification of peak mitochondrial actin intensity normalized to mitochondrial fluorescence intensity. Parental U2OS and TFAM-deficient clones

were compared ($P = 0.0052$ for TF^D-1 and $P = 0.0025$ for TF^D-2). $N = 12$ nucleoids for TF^D-1 and $N = 13$ nucleoids for TF^D-2, representing the total of enlarged nucleoids that was present across images of five cells. An equivalent number of normal-sized nucleoids was measured in each cell, and a total of 15 normal-sized nucleoids were measured across 5 control cells (Methods). **f**, Airyscan imaging of a live TFAM-deficient U2OS cell (TF^D-1) expressing an ER-targeted actin nanobody to label ER actin accumulation (AC-ER). Scale bar, 10 μm and inset scale bars, 1 μm. **g**, Quantification of peak ER actin intensity normalized to ER fluorescence intensity. Parental U2OS and TFAM-deficient clones were compared ($P = 0.09067$ for TF^D-1 and $P = 0.6431$ for TF^D-2). For all conditions in **g**, 15 nucleoids were measured across five cells, except for enlarged nucleoids in U2OS cells ($N = 4$ nucleoids) and normal nucleoids in TF^D-1 cells ($N = 13$ nucleoids). Data in **b**, **e** and **g** were quantified from one representative experiment of three. All differences were compared using an unpaired, two-tailed Student's *t*-test. All plotted lines represent the mean. Source numerical data are available in Source data.
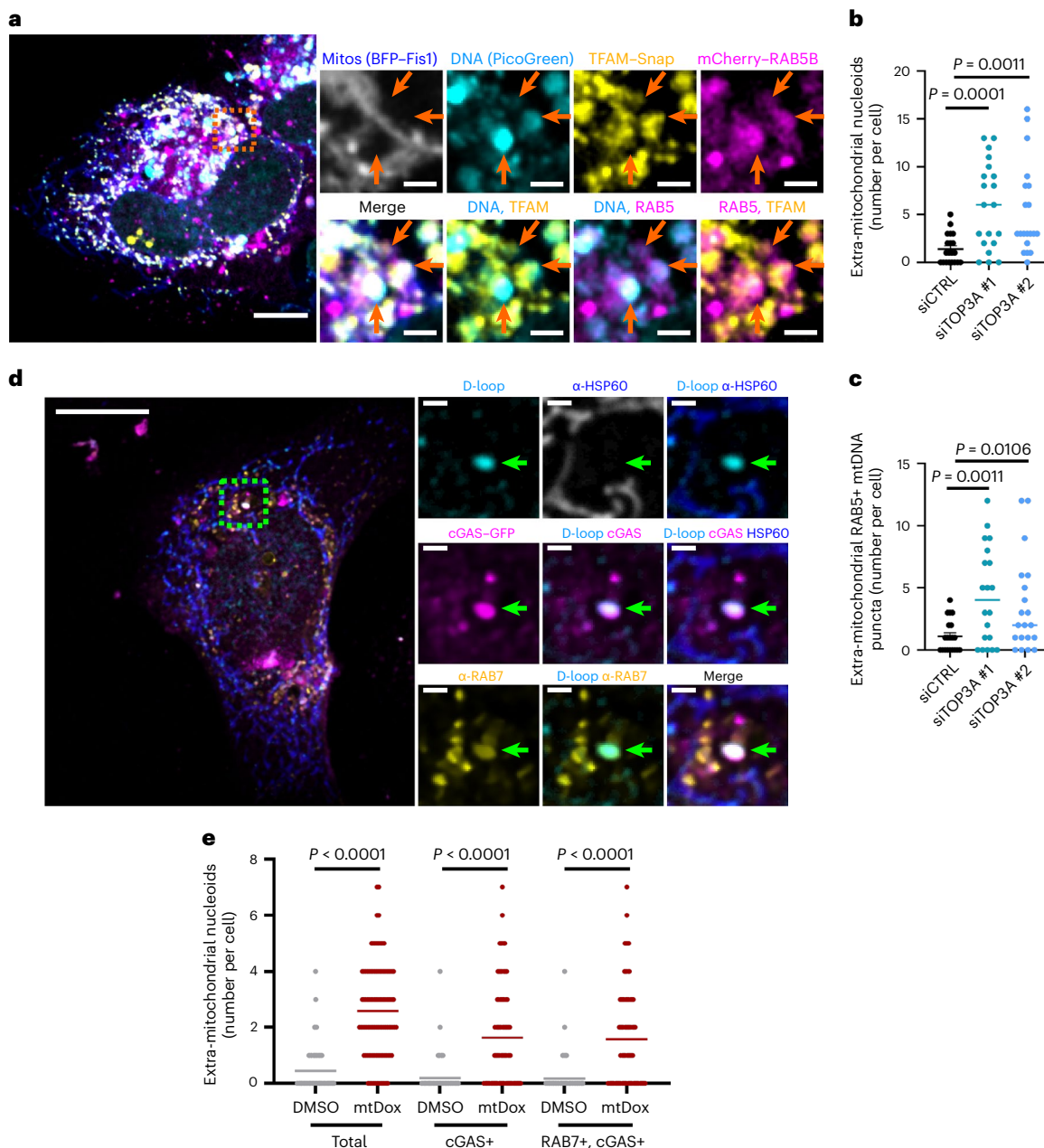
Fig. 8 | Loss of mtDNA segregation or mtDNA damage triggers endosomal trafficking of nucleoids. a, Confocal imaging of a live U2OS cell depleted of TOP3A (siRNA #1), labelled with PicoGreen, and expressing TFAM–SNAP, mCherry–RAB5B and BFP–Fis1. Scale bar, 10 μm and inset scale bars, 2 μm. **b**, The number of extra-mitochondrial nucleoids (non-mitochondrial PicoGreen also positive for TFAM–SNAP) per cell was scored. siCTRL was compared with TOP3A siRNAs #1 (*P* = 0.0001) or #2 (*P* = 0.0011). **c**, The number of extra-mitochondrial nucleoids also positive for mCherry–RAB5B was scored. siCTRL was compared to TOP3A siRNAs #1 (*P* = 0.0011) or #2 (*P* = 0.0106). For both **b** and **c**, *N* = 20 cells for all conditions. Data were pooled from three independent

experiments. **d**, Spinning disk imaging of mtDNA FISH (D-loop probe), followed by immunofluorescence against HSP60 and GFP, in U2OS cells that were transfected with cGAS–GFP and then treated with either dimethylsulfoxide (DMSO) or mtDox (10 μM). Scale bars, 20 μm and inset scale bars, 2 μm. **e**, The number of extra-mitochondrial nucleoids that overlapped with cGAS–GFP and RAB7 was scored. DMSO was compared with mtDox (*P* < 0.0001). *N* = 110 cells for DMSO and *N* = 101 cells for mtDox. Data were pooled from three independent experiments. All differences were compared using an unpaired, two-tailed Student's *t*-test, and all plotted lines represent the mean. Source numerical data are available in Source data.

mitochondrial actin polymerization occurring first[40]. Using previously characterized organelle-specific actin probes[40], we observed enrichment of mitochondrial-associated actin at the sites of enlarged nucleoids (Fig. 7d,e), but no obvious accumulation of ER-associated actin (Fig. 7f,g). These data indicate that TFAM-deficient cells are halted at an intermediate stage of mitochondrial fission, between the completion of the final steps of mtDNA replication and initiation of ER actin polymerization.

The results above led us to consider that it is mtDNA replication stress that halts mitochondrial fission, preventing the segregation of nucleoids that have not completed the final stages of mtDNA replication. To directly test this hypothesis, we depleted cells of TOP3A, which mediates decatenation and physical separation of mitochondrial genomes following the completion of mtDNA synthesis[41]. TOP3A depletion (Extended Data Fig. 9a) led to the formation of enlarged nucleoids (Extended Data Fig. 9b), as previously described[41], and

these enlarged nucleoids localized to mitochondria–ER contact sites (Extended Data Fig. 9c,d). As is the case during TFAM depletion or HSV-1 UL12.5 expression, TOP3A depletion caused mitochondrial elongation (Extended Data Fig. 9e,f). This effect is consistent with a decrease in mitochondrial fission driving nucleoid escape from mitochondria and ultimate cGAS–STING activation via their entry into the endolysosomal pathway that we propose (Fig. 4a), though we cannot also rule out a contribution from an increase in the rates of mitochondrial fusion to the resulting mitochondrial morphology arising from TOP3A depletion. Importantly, TOP3A depletion triggered mtDNA release into RAB5-marked endosomes (Fig. 8a–c), further indicating that the inability of nucleoids to complete segregation triggers their exit from mitochondria and trafficking within endosomes. Finally, we caused physical damage to mtDNA by treating wild-type cells with mitochondria-targeted doxorubicin that we showed previously increases expression of ISGs[3,42], and found that this too is sufficient to trigger the release of enlarged nucleoids and their colocalization with both RAB7 and cGAS (Fig. 8d,e).

Discussion

On the basis of our results, we propose that mtDNA damage and/or other stressors that prevent the completion of mtDNA replication or segregation instigate a late mitochondrial fission checkpoint that ensures the inheritance of intact, non-damaged mtDNA molecules in each daughter mitochondrion after mitochondrial division. Furthermore, we propose that prolonged engagement of this mitochondrial fission checkpoint leads to the removal of these defective nucleoids and trafficking to endosomes to rectify the situation. However, this emergency response is prone to cGAS–STING activation via rupture of mtDNA-containing late endosomes. There is a fast-growing list of pathways in addition to mitophagy that maintain mitochondrial homeostasis, including MDVs[17–19], and piecemeal removal and degradation of mitochondrial components such as nucleoids[23] and MICOS complexes[43]. Furthermore, it was recently demonstrated that mitophagy suppresses mtDNA-driven inflammation, and that MDVs can promote the release of immunostimulatory mtDNA[18,44], pointing to an important nexus between mitochondrial quality control and innate immune signalling pathways. In this regard, our results add to an exciting, emerging theme that endosomes mediate mtDNA[23] and mitochondria[22,25,45] quality control. We demonstrate not only that replication-incompetent nucleoids are trafficked to endosomes for disposal, but that this type of dysfunctional mtDNA can activate cGAS when endosomes rupture. Elucidating the precise mechanisms that enable RAB5-dependent relocalization of nucleoids to endosomes is an important future direction. We propose that this endosome–mtDNA release pathway is separate from that mediated by BAK/BAX[14,15] pores, VDAC pores[16] or MDVs[18]. Going forward, it will be important to characterize which of these mtDNA-release mechanisms, and perhaps others yet to be discovered, operate under different physiological and pathological contexts. That we observe endosomal-mediated mtDNA release during HSV-1 infection suggests that this pathway is probably relevant to the other viral infections where mtDNA release has been reported[2,7]. Finally, our results point to mtDNA replication, mitochondrial fission and the endolysosomal pathway as potential targets to prevent mtDNA release or augment the disposal of immunostimulatory mtDNA to prevent inflammatory pathology associated with multiple diseases and ageing.

Online content

Any methods, additional references, Nature Portfolio reporting summaries, source data, extended data, supplementary information, acknowledgements, peer review information; details of author contributions and competing interests; and statements of data and code availability are available at https://doi.org/10.1038/s41556-023-01343-1.

References

1. Nadalutti, C. A., Ayala-Peña, S. & Santos, J. H. Mitochondrial DNA damage as driver of cellular outcomes. *Am. J. Physiol.* **322**, C136–C150 (2022).
2. Newman, L. E. & Shadel, G. S. Mitochondrial DNA release in innate immune signaling. *Annu. Rev. Biochem.* https://doi.org/10.1146/annurev-biochem-032620-104401 (2023).
3. Wu, Z., Sainz, A. G. & Shadel, G. S. Mitochondrial DNA: cellular genotoxic stress sentinel. *Trends Biochem. Sci.* **46**, 812–821 (2021).
4. Kasashima, K., Sumitani, M. & Endo, H. Human mitochondrial transcription factor A is required for the segregation of mitochondrial DNA in cultured cells. *Exp. Cell Res.* **317**, 210–220 (2011).
5. Bonawitz, N. D., Clayton, D. A. & Shadel, G. S. Initiation and beyond: multiple functions of the human mitochondrial transcription machinery. *Mol. Cell* **24**, 813–825 (2006).
6. Parisi, M. A. & Clayton, D. A. Similarity of human mitochondrial transcription factor 1 to high mobility group proteins. *Science* **252**, 965–969 (1991).
7. West, A. P. et al. Mitochondrial DNA stress primes the antiviral innate immune response. *Nature* **520**, 553–557 (2015).
8. Wu, Z. et al. Mitochondrial DNA stress signalling protects the nuclear genome. *Nat. Metab.* **1**, 1209–1218 (2019).
9. Chatre, L. & Ricchetti, M. Large heterogeneity of mitochondrial DNA transcription and initiation of replication exposed by single-cell imaging. *J. Cell Sci.* **126**, 914 (2013).
10. Moriyama, M., Koshiba, T. & Ichinohe, T. Influenza A virus M2 protein triggers mitochondrial DNA-mediated antiviral immune responses. *Nat. Commun.* **10**, 4624 (2019).
11. Saffran, H. A., Pare, J. M., Corcoran, J. A., Weller, S. K. & Smiley, J. R. Herpes simplex virus eliminates host mitochondrial DNA. *EMBO Rep.* **8**, 188–193 (2007).
12. Duguay, B. A. & Smiley, J. R. Mitochondrial nucleases ENDOG and EXOG participate in mitochondrial DNA depletion initiated by herpes simplex virus 1 UL12.5. *J. Virol.* **87**, 11787–11797 (2013).
13. Andreeva, L. et al. cGAS senses long and HMGB/TFAM-bound U-turn DNA by forming protein–DNA ladders. *Nature* **549**, 394–398 (2017).
14. McArthur, K. et al. BAK/BAX macropores facilitate mitochondrial herniation and mtDNA efflux during apoptosis. *Science* **359**, eaao6047 (2018).
15. Riley, J. S. et al. Mitochondrial inner membrane permeabilisation enables mtDNA release during apoptosis. *EMBO J.* **37**, e99238 (2018).
16. Kim, J. et al. VDAC oligomers form mitochondrial pores to release mtDNA fragments and promote lupus-like disease. *Science* **366**, 1531–1536 (2019).
17. Soubannier, V. et al. A vesicular transport pathway shuttles cargo from mitochondria to lysosomes. *Curr. Biol.* **22**, 135–141 (2012).
18. Zecchini, V. et al. Fumarate induces vesicular release of mtDNA to drive innate immunity. *Nature* **615**, 499–506 (2023).
19. Sugiura, A., McLelland, G.-L., Fon, E. A. & McBride, H. M. A new pathway for mitochondrial quality control: mitochondrial-derived vesicles. *EMBO J.* **33**, 2142–2156 (2014).
20. Fader, C. M. & Colombo, M. I. Autophagy and multivesicular bodies: two closely related partners. *Cell Death Differ.* **16**, 70–78 (2009).
21. Wandinger-Ness, A. & Zerial, M. Rab proteins and the compartmentalization of the endosomal system. *Cold Spring Harb. Perspect. Biol.* **6**, a022616 (2014).
22. Hammerling, B. C. et al. A Rab5 endosomal pathway mediates Parkin-dependent mitochondrial clearance. *Nat. Commun.* **8**, 14050 (2017).
23. Sen, A. et al. Mitochondrial membrane proteins and VPS35 orchestrate selective removal of mtDNA. *Nat. Commun.* **13**, 6704 (2022).

24. Irazoki, A. et al. Disruption of mitochondrial dynamics triggers muscle inflammation through interorganellar contacts and mitochondrial DNA mislocation. *Nat. Commun.* **14**, 108 (2023).

25. Yamano, K. et al. Endosomal Rab cycles regulate Parkin-mediated mitophagy. *eLife* **7**, e31326 (2018).

26. Hsu, F. et al. Rab5 and Alsin regulate stress-activated cytoprotective signaling on mitochondria. *eLife* **7**, e32282 (2018).

27. Hamacher-Brady, A., Choe, S. C., Krijnse-Locker, J. & Brady, N. R. Intramitochondrial recruitment of endolysosomes mediates Smac degradation and constitutes a novel intrinsic apoptosis antagonizing function of XIAP E3 ligase. *Cell Death Differ.* **21**, 1862–1876 (2014).

28. Day, R. A. & Sletten, E. M. Experimental perspectives on direct visualization of endosomal rupture. *ChemBioChem* **22**, 3277–3282 (2021).

29. Lewis, S. C., Uchiyama, L. F. & Nunnari, J. ER–mitochondria contacts couple mtDNA synthesis with mitochondrial division in human cells. *Science* https://doi.org/10.1126/science.aaf5549 (2016).

30. Smirnova, E., Shurland, D. L., Ryazantsev, S. N. & van der Bliek, A. M. A human dynamin-related protein controls the distribution of mitochondria. *J. Cell Biol.* **143**, 351–358 (1998).

31. Smirnova, E., Griparic, L., Shurland, D. L. & van der Bliek, A. M. Dynamin-related protein Drp1 is required for mitochondrial division in mammalian cells. *Mol. Biol. Cell* **12**, 2245–2256 (2001).

32. Labrousse, A. M., Zappaterra, M. D., Rube, D. A. & van der Bliek, A. M. *C. elegans* dynamin-related protein DRP-1 controls severing of the mitochondrial outer membrane. *Mol. Cell* **4**, 815–826 (1999).

33. Ban-Ishihara, R., Ishihara, T., Sasaki, N., Mihara, K. & Ishihara, N. Dynamics of nucleoid structure regulated by mitochondrial fission contributes to cristae reformation and release of cytochrome c. *Proc. Natl Acad. Sci. USA* **110**, 11863–11868 (2013).

34. Manor, U. et al. A mitochondria-anchored isoform of the actin-nucleating spire protein regulates mitochondrial division. *eLife* **4**, e08828 (2015).

35. Chakrabarti, R. et al. INF2-mediated actin polymerization at the ER stimulates mitochondrial calcium uptake, inner membrane constriction, and division. *J. Cell Biol.* **217**, 251–268 (2017).

36. Korobova, F., Ramabhadran, V. & Higgs, H. N. An actin-dependent step in mitochondrial fission mediated by the ER-associated formin INF2. *Science* **339**, 464–467 (2013).

37. De Vos, K. J., Allan, V. J., Grierson, A. J. & Sheetz, M. P. Mitochondrial function and actin regulate dynamin-related protein 1-dependent mitochondrial fission. *Curr. Biol.* **15**, 678–683 (2005).

38. Li, S. et al. Transient assembly of F-actin on the outer mitochondrial membrane contributes to mitochondrial fission. *J. Cell Biol.* **208**, 109–123 (2015).

39. Ji, W. K., Hatch, A. L., Merrill, R. A., Strack, S. & Higgs, H. N. Actin filaments target the oligomeric maturation of the dynamin GTPase Drp1 to mitochondrial fission sites. *eLife* **4**, e11553 (2015).

40. Schiavon, C. R. et al. Actin chromobody imaging reveals sub-organellar actin dynamics. *Nat. Methods* **17**, 917–921 (2020).

41. Nicholls, T. J. et al. Topoisomerase 3α is required for decatenation and segregation of human mtDNA. *Mol. Cell* **69**, 9–23.e6 (2018).

42. Chamberlain, G. R., Tulumello, D. V. & Kelley, S. O. Targeted delivery of doxorubicin to mitochondria. *ACS Chem. Biol.* **8**, 1389–1395 (2013).

43. Abudu, Y. P. et al. SAMM50 acts with p62 in piecemeal basal- and OXPHOS-induced mitophagy of SAM and MICOS components. *J. Cell Biol.* **220**, e202009092 (2021).

44. Sliter, D. A. et al. Parkin and PINK1 mitigate STING-induced inflammation. *Nature* **561**, 258–262 (2018).

45. Puri, C. et al. The RAB11A-positive compartment is a primary platform for autophagosome assembly mediated by WIPI2 recognition of PI3P-RAB11A. *Dev. Cell* **45**, 114–31.e8 (2018).

46. Chatre, L. & Ricchetti, M. in *Mitochondrial Medicine: Volume I, Probing Mitochondrial Function* (eds Weissig, V. & Edeas, M.) 133–147 (Springer, 2015).

Laura E. Newman[1], **Sammy Weiser Novak**[1], **Gladys R. Rojas**[1], **Nimesha Tadepalle**[1], **Cara R. Schiavon**[1], **Danielle A. Grotjahn** [2], **Christina G. Towers** [1], **Marie-Ève Tremblay** [3], **Matthew P. Donnelly**[1,4,5], **Sagnika Ghosh** [1], **Michaela Medina** [2], **Sienna Rocha**[1], **Ricardo Rodriguez-Enriquez** [1], **Joshua A. Chevez**[6], **Ian Lemersal**[7], **Uri Manor** [1,6,8] & **Gerald S. Shadel** [1]

[1]Salk Institute for Biological Studies, La Jolla, CA, USA. [2]The Scripps Research Institute, La Jolla, CA, USA. [3]University of Victoria, Victoria, British Columbia, Canada. [4]Medical Scientist Training Program, University of California, San Diego, La Jolla, CA, USA. [5]Biomedical Sciences Graduate Program, University of California, San Diego, La Jolla, CA, USA. [6]Division of Biological Sciences, University of California, San Diego, La Jolla, CA, USA. [7]La Jolla Institute for Immunology, La Jolla, CA, USA. [8]Department of Cell & Developmental Biology, University of California, San Diego, La Jolla, CA, USA. e-mail: uri@ucsd.edu; gshadel@salk.edu

Methods

Animal strains and cell lines

All animal husbandry and procedures were institutional animal care and use committee approved by the animal care and use committees at Yale University or the Salk Institute for Biological Studies. $Tfam^{+/-}$ mice were originally derived from $Tfam^{flox}$ mice obtained from N. Chandel (Northwestern University) and generated as described previously[7,47]. IMR-90 human foetal lung fibroblasts and $Bak^{-/-}Bax^{-/-}$ MEFs were purchased from American Type Culture Collection (ATCC). TFAM-deficient U2OS cell lines were derived from a CRISPR-knockout pool of U2OS cells (purchased from Synthego) by using limiting dilution to obtain single-cell clones. Editing of TFAM was confirmed by sequencing (Extended Data Fig. 2). The parental U2OS line from the ATCC was supplied alongside the CRISPR pooled cells and used in all experiments. All experiments using CRISPR-mediated knockout were performed using two independent clones, TF^D-1 (clone number 5G8) and TF^D-2 (clone number 1C11), to guard against clonal as well as off-target CRISPR differences.

Cell culture

Wild-type and $Tfam^{+/-}$ MEFs were generated from mouse embryos isolated between embryonic day 12.5 and 14.5 and cultured in Dulbecco's modified Eagle medium (DMEM; Corning), supplemented with 10% foetal bovine serum (FBS; Gibco, Thermo Fisher). All experiments were performed in primary MEFs passaged five or fewer times. IMR-90 cells were obtained from the ATCC and were cultured in Eagle's minimal essential medium supplemented with 10% FBS and were not used for experiments past 30 population doublings. Immortalized cell lines were not used for experiments beyond passage 30. TFAM-deficient U2OS clones as well as parental U2OS cells were cultured in DMEM supplemented with 10% FBS. To generate stable TFAM short hairpin (sh)RNA cell strains, LentiCRISPRv2 vector with predesigned shRNA (Sigma mission shRNA TRCN0000312779, target sequence TGTCAAACTAGAACGGA-TAAA) (3 μg) was transfected into Lenti-x 293T cells (50–60% density in 6 cm^2 dishes) along with 2.25 μg psPAX2 and 0.75 μg pMD2.G plasmids using Lipofectamine 2000 (cat. no. 12566014, Thermo Fisher) at a ratio of 1:1 (Lipofectamine 2000/nucleic acid (μg)) to produce lentivirus. Lentivirus-containing media were collected 48 h post-transfection and filtered using a 0.45 μm membrane. $Bak^{-/-}Bax^{-/-}$ (ATCC) or wild-type immortalized MEFs were infected with lentivirus for 24 h and then selected for antibiotic resistance in 20 μg ml^{-1} blasticidin for 5 days. For all imaging experiments, fibronectin coating was achieved by incubating dishes with fibronectin (10 μg ml^{-1}) diluted from stock solution (cat. no. F1141, Sigma). For experiments with HSV-1–GFP[48] and HSV-1–mCerulean[49], U2OS cells were infected at multiplicity of infection of 10 in phosphate-buffered saline (PBS; cat. no. 14190250, Thermo Fisher) for 1 h with gentle shaking, after which point growth medium was added, and the cells were fixed or imaged at the indicated timepoints. For all experiments, cells were targeted for a final density of 50–70%, and variations in cell density between experimental conditions were minimized. All cells were screened monthly for mycoplasma (cat. no. LT07-418, Lonza). Additional mycoplasma screening was regularly performed by staining cells with Hoescht 33342 during imaging experiments, whenever possible.

Plasmids

The following plasmids were purchased from Addgene: TOMM20–mCherry (55146), TOM20–Halo (111135), mtBFP (55248), AIF–mCherry (67530), mTurquoise–LC3 (55579), mCherry–RAB5B (49201), GFP–Galectin 8 (127191), psPAX2 (12260) and pMD2.G (12259). AC-Mito, Halo-Mito, AC-ER and Halo-ER were previously described, using tail anchor sequences from either Fis1 (mitochondria) or CytB5 (ER) for targeting[40]. Human cGAS fused to EGFP in pcDNA3.1(+) was purchased from Genescript, and mCherry or Halo was subcloned in place of EGFP. To generate EBFP–Fis1 and Halo–Fis1, EBFP or Halo was subcloned into the mCherry–Fis1 construct that was previously described

(mCherry–Mito[40]). HSV-1 UL12.5 was purchased from Addgene (cat. no. 70109) and the EGFP was removed by subcloning. Constructs directing the expression of UL12.5 along with NLS–GFP (as a marker) were purchased from Vector Builder and used in Fig. 3j and Extended Data Fig. 4e. Ii33–mCherry was a generous gift from Dr P. Satpute (Uniformed Services University of the Health Science), RAB7A–GFP[50] was a generous gift from Dr Chengbiao Wu (University of California, San Diego), and TFAM–SNAP was a generous gift from Dr Jodi Nunnari (Altos).

Transfection

Transfection of siRNAs (Supplementary Table 2, purchased from Integrated DNA Technologies (IDT)) into MEFs, U2OS and IMR-90 at 50–70% density was achieved using Lipofectamine RNAiMax (cat. no. 1847641, Invitrogen), according to the manufacturer's instructions. All siRNAs were transfected at a final concentration of 25 nM. Following 24 h of transfection, cells were passaged (typically 1:8 or 1:10 to achieve a target final density of 50–70%) into new dishes or onto fibronectin-coated coverslips and collected 96 h from the start of transfection. For IMR-90 cells, both the new plates (for quantitative PCR (qPCR)/western blot experiments), as well as coverslips, were coated with freshly prepared fibronectin solution to receive cells passaged immediately after transfection. Transfection of plasmid DNA was performed using Lipofectamine 2000 (cat. no. 12566014, Thermo Fisher) at a ratio of 4:1 (Lipofectamine 2000/nucleic acid (μg)), according to the manufacturer's instructions. Confluent U2OS cells were transfected with 2 μg in one well of a six-well plate. When transfecting multiple plasmids, the amount of plasmid transfected was evenly split to reach a final amount of 2–2.5 μg for all plasmids, with the exception of fluorescent proteins with emission in the blue range, for which the amount of plasmid DNA was doubled relative to the other plasmids. Following 4 h of transfection in growth medium, cells were trypsinized and plated onto coverslips (1:2 split) or Nunc eight-well chamber slides (cat. no. 155409PK, Thermo Fisher) (20,000–40,000 cells per well).

Live cell imaging

Cells were imaged in eight-well chamber slides (cat. no. 155409PK, Thermo Fisher). Cells were labelled with the following dyes: PicoGreen (1:500, cat. no. P11495, Thermo Fisher), Mitotracker Red or Deep Red (100 nM, cat. nos. M7512 and M22426, Thermo Fisher) and LysoTracker Deep Red (50 nM, cat. no. L12492, Thermo Fisher). Cells were incubated with dyes for 30 min, followed by three washes with PBS. For experiments with LysoTracker Deep Red, bafilomycin A1 (200 nM, cat. no. B1793, Sigma) was included as a negative control, and cells were incubated with bafilomycin A1 for 15 min before labelling, during LysoTracker labelling and throughout the imaging experiment. Cells were imaged in live cell medium composed of phenol-red free DMEM (cat. no. 921-063-02, Thermo Fisher) supplemented with Prolong Antifade (cat. no. P36975, Thermo Fisher) and 10% FBS. Janelia Fluor 635 (250–500 nM) was added to the live cell medium if a Halo-tagged construct was expressed. The SNAP tag was labelled with 647-SiR (cat. no. S9102S, New England Biolabs), according to the manufacturer's instructions.

Immunofluorescence and FISH

Cells grown on fibronectin-coated coverslips (cat. no. 12-545-81, Fisher Scientific) were fixed at 37 °C using a pre-warmed (37 °C) solution of 4% paraformaldehyde in PHEM buffer (60 mM 1,4-Piperazinediethanesulfonic acid (PIPES), 25 mM 4-(2-Hydroxyethyl) piperazine-1-ethanesulfonic acid (HEPES), 10 mM Ethylene-bis-(oxyethylenenitrilo)tetraacetic acid (EGTA) and 4 mM MgSO$_4$, pH 6.8) for 15 min, and then permeabilized with 0.1% (vol/vol) Triton X-100 in PBS for 10 min at room temperature. FISH was then performed as previously described[46]. Probes #4 and #8 were prepared as previously described, and the mREP probe conjugated to Atto550 or Atto633

(ref. 46) was purchased from IDT. FISH probes were not used past one freeze/thaw cycle to preserve signal. A FISH probe against mouse D-loop was similarly purchased (IDT) and used in Extended Data Fig. 3d (sequence: TAACTCTCCAAACCCCCCCACCCCCTCCTCTTAATGC-CAAACCCCAAAAACACTAAGAACTTGAAAGACATATAATATTAAC-TATCAAACCCTATGTCCTG). We verified that all FISH probes were specific to mtDNA by treating permeabilized coverslips with protein-ase K followed by DNase I to digest mtDNA before FISH as previously described[9,46], which resulted in a loss in mitochondria-localized FISH signal. For immunofluorescence, coverslips were blocked with filtered PBS containing 1% (wt/vol) bovine serum albumin (BSA) at room temperature for at least an hour, following either permeabilization with 0.1% Triton X-100 or FISH. Incubation with primary antibodies was carried out in PBS containing 1% (wt/vol) BSA at 4 °C overnight, followed by 4× 5 min washes in PBS. Secondary antibodies (1:500, Thermo Fisher Alexa fluorophores 488, 568 and 647) were incubated in PBS containing 1% BSA for 1 h at room temperature. The second-ary antibody was removed by 4× 5 min washes in PBS. Coverslips were then mounted onto slides using Prolong Glass (cat. no. P36980, Thermo Fisher). The following adjustments were made for particular experiments. If the anti-DNA primary antibody was used, washes following primary incubation were instead performed using 5 mM ethylenediaminetetraacetic acid (EDTA) in PBS, as we found that it effectively removed the background associated with that particular antibody. If FISH was performed before immunofluorescence, the concentration of primary antibodies was doubled, to account for loss of signal caused by denaturation. Additional controls were included with FISH experiments, including the use of a coverslip that did not receive FISH probe, as a readout for background signal, as well as the inclusion of immunofluorescence against DNA to judge colocalization with FISH signal, whenever possible. When four-colour imaging was performed, HSP60 was imaged in the blue channel, and the concentra-tion of both primary (HSP60, 1:500) and secondary antibodies (Alexa 405, 1:250) was increased. Similarly, both primary (RAB7, 1:50) and secondary antibody (Alexa 750, 1:250) concentrations were doubled when imaging with 730 nm laser excitation. To visualize Twinkle, antigen retrieval was performed before permeabilization by heat-ing coverslips to 95 °C in antigen retrieval buffer (100 mM Tris, 5% (wt/vol) urea, pH 9.5) for 10 min, followed by 4× 5 min washes in PBS. Immunofluorescence was then performed using freshly purchased anti-Twinkle antibody.

The following antibodies were obtained commercially and used at the indicated dilutions for immunofluorescence: TOM20 (cat. no. 612278, BD Biosciences, 1:1,000), TOMM20 (cat. no. ab186734, Abcam, 1:200), cGAS (cat. no. 15102, CST, 1:100), TFAM (cat. no. 22586-1-AP, Pro-teintech, 1:500), TFAM (cat. no. ab119684, Abcam, 1:250), DNA (cat. no. CBL186, Millipore, 1:200), HSP60 (cat. no. 12165, CST, 1:1,000), HSP60 (cat. no. CPCA-HSP60, EnCor Biotechnology, 1:1,000), LC3A/B (cat. no. 12741T, CST, 1:100), Twinkle (cat. no. ab83329, Abcam, 1:100), POLG2 (cat. no. 10997-2-AP, Proteintech, 1:100), mtSSB (cat. no. 12212-1-AP, Proteintech, 1:100), RAB7 (cat. no. 9367, CST, 1:100) and activated BAX (cat. no. sc-23959, Santa Cruz Biotechnology, 1:100). Secondary anti-bodies conjugated to Alexa 405, 488, 568, 647 or 750 were purchased from Thermo Fisher, with the exception of anti-chicken 647, which was from Abcam.

EdU incorporation
EdU experiments were performed using the Alexa 488 Click-It EdU kit (cat. no. C10637, Thermo Fisher), with the following modifications to the manufacturer protocol. Cells on coverslips were incubated with EdU (50 µM) for 4 h before fixation. After fixation, two sequential, hour-long click reactions were performed, using a freshly made solu-tion for each reaction. Coverslips were then washed three times with 3% BSA in PBS, after which point immunofluorescence was performed as described above.

Microscopy
For all experiments, 405, 488, 561 and 633 nm laser lines were used. For all fixed-cell imaging, images shown are maximum intensity z projec-tions, unless otherwise noted. For Airyscan imaging, fixed cells were imaged with a Plan-Apochromat 63×/1.4 numerical aperture (NA) oil objective on an upright Zeiss 880 LSM Airyscan confocal microscope. Live cells were imaged with a Plan-Apochromat 63×/1.4 NA oil objective on an inverted Zeiss 880 LSM Airyscan confocal microscope with the environmental control system supplying 37 °C, 5% CO$_2$ and humidity. For time-lapse imaging, the zoom factor was set to 3–4× to increase the frame rate. In all cases, the maximum pixel-dwell time (~0.684 µs per pixel) and 2× Nyquist optimal pixel size (~40 nm per pixel) was used. Airyscan data were processed using Zen Black (Zeiss, version 2.3). For all Airyscan live cell images, single planes are shown. Airyscan images are denoted as 'Airyscan images' in the figure legends. For images denoted as 'spinning disk imaging' in figure legends, fixed and live cell imaging was performed using a Zeiss CSU spinning disk confocal micro-scope with a Confocal Scanner Unit-X1 Yokogawa spinning disk scan head on a Prime 95B scientific complementary metal oxide semicon-ductor (sCMOS) camera (Teledyne Photometrics), using an inverted Plan-Aprochromat 63×/1.4 NA oil objective. When mCherry–RAB5B was imaged in live cells, acquisition times for z stacks were limited to ~45 s to minimize motion artefacts. For the experiment in Fig. 3j, imaging of fixed cells was performed on an Olympus FV3000 confocal microscope using a 60×/1.5 NA oil objective, using Galvano detection and Nyquist sampling. Samples were excited with 405, 488, 561 and 750 nm lasers, followed by sequential excitation with a 633 nm laser. For the experiments in Fig. 4h and Extended Data Figs. 4e and 6c, the Olympus FV3000 microscope was used with resonant scanning detec-tion and 405, 488, 561 and 633 nm lasers, and the zoom was set to 3.5x, which slightly under-sampled images but increased acquisition speed. To prevent bleedthrough from LysoTracker Deep Red (Extended Data Fig. 6c), acquisition in the green channel was limited to 500–520 nm, and the red channel was avoided. For the experiments shown in Extended Data Figs. 7a and 8h, imaging of fixed cells was performed using an HCX Plan-Apochromat 100×/1.4 NA CS oil objective on an inverted Leica SP5 microscope.

Correlative live cell imaging and 3D SEM
All consumable materials for electron microscopy (EM) sample prepa-ration were sourced from Electron Microscopy Sciences unless other-wise noted. TFAM-deficient U2OS cells were transfected as described above with cGAS–mCherry, TOM20–Halo and mTurquoise–LC3 and plated onto gridded coverslips in 35 mm dishes (cat. no. D35-14-1.5GI, Cellvis). Cells were stained with PicoGreen and JF635 as described in the cell culture section. The PicoGreen, cGAS–mCherry and TOM20–Halo channels were imaged live as described above until an apparent mtDNA release event occurred, which defined ROIs for EM imaging. Samples were then fixed while imaging on the microscope by adding dropwise an equal volume of 2× EM fixative (5% glutaraldehyde and 4% paraformaldehyde in 0.1 M cacodylate buffer with 3 mM CaCl$_2$) warmed to 37 °C, to the live cell medium already in the dish. After fixa-tion, oversampled z stacks (100 nm step size) were collected of all four channels. Additional images of the surrounding cells and the grid were also acquired to aid in relocating the cell. Samples were immediately removed from the microscope, fixative-medium solution was dis-carded, and cells were washed once and left in fresh ice-cold 1× fixative for at least 60 min and rinsed three times with ice-cold 0.1 M cacodylate buffer with 3 mM CaCl$_2$. Coverslips were post-fixed and stained with 1.5% reduced osmium for 35 min, rinsed five times with MilliQ water, and stained again with 1% aqueous uranyl acetate for 1 h at room tem-perature, before serial dehydration with graded solutions of ice-cold ethanol in water. Samples were then fully dehydrated in two 10 min rinses of anhydrous ethanol at room temperature before infiltration with Durcupan resin. After 3:1, 1:1 and 1:3 ethanol-resin 2 h infiltration

steps, samples were infiltrated with pure resin for 2 h before another change of fresh pure resin and left overnight at room temperature. In the morning, a final change of fresh resin was performed, taking care to let the viscous resin fully drain by inverting the coverslip before adding the final aliquot of fresh resin from the edge of the dish. Resin was added to fill the dish up to 2 mm and infiltrated samples were polymerized for 48 h at 65 °C. After polymerization, coverslips were dissolved by floating a drop of concentrated hydrofluoric acid on the glass for 15 min and rinsing thoroughly with water. CLEM was achieved using laser-branded fiducials in a thinly embedded sample, as previously described[51]. Briefly, ROIs were identified by their grid positions and dark osmium staining. ROIs were marked using the high-powered ultraviolet cutting laser of a Zeiss Palm laser capture dissection microscope to provide orientation and fiducial guides for further trimming and ultramicrotomy. Following laser cutting, an additional protective layer of resin was applied. ROIs were carefully identified under a dissecting microscope and excised from the coverslip using a jeweller saw and a scalpel, with careful thought given to the future blockface orientation. The small ($1 \times 2 \times 2$ mm) sample block was glued to a blank resin block such that the ROIs were orthogonal to the cutting plane and approximately 100 µm from the cutting surface. Laser marks on the block face helped to identify the location of the ROI using the ultramicrotome optics. The block was carefully trimmed using a 90° diamond trimming knife (Diatome) so that the block width bounded the fiducial laser marks, and the two sides of the block face were perfectly parallel for serial sectioning when turned 90°. The ROI was approached using the trimming knife to provide a perfectly smooth block face. When the fiducials marking the location the of ROI became challenging to visualize (about 5–15 µm from the blockface), a diamond knife with a water boat appropriate for serial sectioning (Histo 45°, Diatome) was installed on the ultramicrotome and 70 nm serial sections were collected on a series of plasma cleaned custom-diced silicon chips (University Wafer) immersed in the knife boat. The chips were mounted on aluminium stubs using double-sided carbon sticky tape and loaded into a Zeiss Sigma VP scanning electron microscope. Chip mapping and the imaging of serial sections was facilitated by SmartSEM (Zeiss) software and the Atlas 5 (FIBICS) software packages. Maps of all the serial sections on the silicon chips were collected at 500 nm px^{-1}. Laser marks could be identified in the resin boundary at low magnification, demarcating the ROI in each section. The ROI was identified and captured across 32 serial section scanning electron micrographs. ROIs were imaged at 2 nm px^{-1} using a backscattered electron detector (Gatan). In high-vacuum mode, a 3 keV beam in high-current mode with a 30 µm aperture at a working distance of 9 mm was found to produce signal from which we could resolve the ultrastructure of double membraned organelles (for example, mitochondrial inner and outer membranes) and fine cytoskeletal elements (for example, microtubule). Sections were aligned using Photoshop (Adobe) and registration functions embedded in Fiji (National Institutes of Health (NIH))[52]. The orthogonal projection (for example, x–z) of the SEM data was used to correlate the fluorescence data and produce a common coordinate system using Imaris software (version 9.9, Bitplane).

Correlative light and FIB–SEM

U2OS cells were transfected with UL12.5, cGAS–mCherry, TOM20–Halo (labelled by JF635) and mTurquoise–LC3, and plated onto gridded coverslips in 35 mm dishes (cat. no. D35-14-1.5GI, Cellvis). Samples were fixed by adding dropwise an equal volume of 2× EM fixative (5% glutaraldehyde, 4% paraformaldehyde in 0.1 M cacodylate buffer with 3 mM CaCl$_2$) warmed to 37 °C to the medium already in the dish. The fixative–medium solution was discarded, and cells were washed once and left in fresh ice-cold 1× fixative for at least 60 min and rinsed three times with ice-cold 0.1 M cacodylate buffer with 3 mM CaCl$_2$. After fixation, samples were imaged using a Plan-Apochromat 63×/1.4 NA oil objective on an inverted Zeiss 880 LSM Airyscan confocal microscope to identify

cells with released TFAM–GFP colocalized with cGAS–mCherry but not TOM20–Halo. Samples were then immediately processed for EM, as described above. After polymerization of the Durcupan resin, coverslips were again dissolved by immersion in concentrated hydrofluoric acid, and the entire gridded region of the coverslip was carefully cut out using a fine kerf saw. The resin wafer was mounted for correlative FIB–SEM, as described previously[53] with some modifications. Briefly, the resin wafer was secured to an aluminium SEM pin with the gridded side up using silver adhesive paint and baked at 70 °C overnight. The mounted sample was then sputter coated with a thin layer (about 20 nm) of platinum using a Leica SCD500 sputter coater to mitigate charging from the electron beam. The sample was then loaded into a Zeiss Crossbeam 350 for imaging with Zeiss SmartSEM software. Overview imaging was conducted between 1 and 20 kV at varying working distances using the SE2 and InLens detectors, to reveal both the superficial grid pattern and locations of the underlying cells. The grid position of interest identified from the light microscopy imaging was located and centred. The sample was rotated to account for the desired approach angle for FIB–SEM sequential milling and imaging. The eucentric position was determined and the sample was tilted to 54° and moved to the coincident working distance between the SEM and FIB beam for further processing. A coarse trench was milled part-way through the cell of interest using a FIB current of 15 nA and a 20 µm depth and polished with a FUB current of 3 nA, revealing a cross-section of the cell for evaluation. The rest of the sample preparation and imaging was performed in ATLAS5 control software (Fibics Inc.) using the 3D Tomography Module. Briefly, a platinum pad with fiducial marks was deposited on top of the rest of the cell, autofocus routines were initialized and validated, and the blockface was sequentially imaged and milled with a voxel resolution of $4 \times 4 \times 20$ nm (x–y–z). The total volume collected was $25.5 \times 3 \times 26.6$ µm (x–y–z) or approximately 6.34×10^9 voxels. Data were acquired with the simultaneous operation of the FIB at 50 pA and the SEM at 1.5 kV using a 30 µm aperture. Images were collected using the Zeiss InLens detector. The image stack was aligned using rigid registration functions and a 0.8 px–kernel Gaussian filter was applied to the dataset in ImageJ. The LM and FIB–SEM datasets were correlated independently in Imaris (Supplementary Video 1) and using BigWarp[54], facilitating the unambiguous identification of TFAM+ and cGAS+ structures in the FIB–SEM data. Mitochondria were segmented automatically using Empanada and proofread using VAST Lite. TFAM+ and cGAS+ structures and the nucleus were segmented manually using VAST Lite. All segmented objects were exported as meshes from VAST Lite and imported into Blender software (version 2.79; Blender.org) for further processing and visualization. The BlendGAMer addon was used to quantitatively fix and smooth the object meshes[55] and the Neuromorph addon was used to superimpose models with the dataset[56]. Blender was used for further visualization and animation (Supplementary Video 2).

Cellular cryo-electron tomography data acquisition and tomogram reconstruction

Immortalized *Tfam*$^{+/-}$ MEFs (TFAM Het MEF) and mouse embryonic fibroblasts (SV40 MEF) were cultured on R ¼ carbon 200 mesh gold electron microscopy grids (Quantifoil Micro Tools) and plunge frozen in a liquid ethane/propane mixture using a Vitrobot Mark 4 (Thermo Fischer Scientific). Thin (120–200 nm) vitrified lamellae were prepared by focused ion beam milling using an Aquilos dual-beam FIB–SEM instrument (Thermo Fisher Scientific) following a modified version of a previous manual cryo-preparation workflow[57]. Grids containing lamellae were transferred into a 300 keV Titan Krios microscope (Thermo Fisher Scientific) with a K2 Summit direct electron detector camera (Gatan). Low-magnification tilt series were acquired using SerialEM software[58] with 2° steps between −60° and +60°. Individual tilts were collected with a pixel size of 7.151 Å and a defocus range of −25.9 to −28.1. The dose per tilt was 0.189 e$^-$ Å^{-2}, and the total accumulated dose

for the tilt series was under 11.5 e$^-$ Å^{-2}. Regions of MVBs were selected for high-magnification data collection. High-magnification tilt series were acquired using SerialEM software with 2° steps between −60° and +60°. Individual tilts were collected with a pixel size of 3.106 Å and a defocus range of −15.0 to −17.2. The total dose per tilt was 0.905 e$^-$ Å^{-2}, and the total accumulated dose for the tilt series was under 55 e$^-$ Å^{-2}. The alignment of tilt series was performed in IMOD[59] using patch tracking. Cryo-tomograms were reconstructed using weighted back projection in IMOD.

Quantification of MVBs in tomograms

High-magnification tomograms were used for the quantification of MVBs. MVBs were identified as non-mitochondrial multi-membrane structures in tomograms and were counted only if >1/2 of the MVB was visible in the field of view of the tomogram to avoid overlapping picks. The total number of MVBs was counted per individual tomogram in each condition. Total tomograms for wild type SV40 MEF $N = 15$ and TFAM Het $N = 27$. Mean values for MVB in wild type SV40 MEF of 0.66 and TFAM Het of 1.03.

QPCR

To quantify messenger RNA transcript abundance, RNA was extracted from cells in 6-cm dishes using the RNeasy kit (cat. no. 74106, Qiagen) according to the manufacturer's instructions. The optional steps were included during RNA extraction, and elution time during was extended to 10 min to improve yield. Reverse transcription was achieved using the High Capacity cDNA Kit (cat. no. 4368814, Thermo Fisher) with 2 µg RNA input into each reaction. Complementary DNA (18 ng µl^{-1}) and the indicated primers (Supplementary Table 1, purchased from Eaton Biosciences, 5 µM each of forward and reverse primers) were used for qPCR reactions using Fast SYBR Green Master Mix (cat. no. 4364346, Thermo Fisher). For each biological sample, three technical replicates were performed and normalized against the *Beta actin* or *Gapdh* threshold cycle (Ct) value to calculate ΔCt. The ΔCt of each sample was then compared with the ΔCt of the control sample to generate the ΔΔCt value. Relative expression was then analysed using the $2^{-\Delta\Delta Ct}$ method and the relative fold change was plotted with the control samples given a value of 1.0. Of the triplicate measurements, outliers were discarded only if different from the average of the other two values by greater than 0.5 cycles. To quantify mtDNA, cells were suspended in 50 mM NaOH and boiled (95 °C) for 1 h followed by neutralization by 1/10 final volume of 1 M Tris–HCl (pH 8.0). DNA samples were diluted to 10 ng µl^{-1} and subjected to qPCR analysis using D-loop and ND4 primers (Supplementary Table 1) to amplify mtDNA, and 18S primers (Supplementary Table 1) to amply nDNA. Three technical replicates were performed for each biological sample and normalized against the nuclear 18S value. Relative copy number was analysed using a $2^{-\Delta\Delta Ct}$ method, and the control mtDNA abundance was given a value of 100%.

Western blotting

Protein samples (20–30 µg per well) were separated on 8–16% precast polyacrylamide gels (cat. no. 4561106, Bio-Rad) and transferred to polyvinylidene difluoride membranes (cat. no. IPVH00010, EMD Millipore) using Tris-glycine transfer buffer (cat. no. 12539, CST) for 1 h at 100 V. TOP3A blots were transferred in Tris-glycine transfer buffer plus 0.01% sodium dodecyl sulfate. Western blotting procedures were carried out at room temperature. Membranes were blocked with either 5% BSA in Tris-buffered saline plus 0.1% Neonate-20 (TBST) (cat. no. J63711, Thermo Fisher) or 5% milk in TBST (for TOP3A antibody) for 1 h. Removal of excess primary antibody was carried out by washing the membranes in TBST three times for 5 min each. Secondary antibodies (cat. nos. 7076P2 and 7074P2, CST, 1:2,000) were diluted in 5% BSA in TBST and incubated with the membrane for 90 min. at room temperature. Excess secondary antibody was removed by washing the membranes in TBST three times for 10 min. each. Membranes were

exposed to Clarity ECL reagent (cat. no. 1705060, Bio-Rad), for 5 min. at room temperature and then visualized using a Chemidoc gel imager (Bio-Rad). Protein normalization was carried out using horseradish peroxidase-conjugated anti-β-actin at a dilution of 1:1,000 (cat. no. 5125S, CST). Western blots were quantified using Fiji, with normalization to both β-actin and the control siRNA condition, and control samples were given a value of 1. The following antibodies were used for western blotting: TFAM (cat. no. 22586-1-AP, Proteintech, 1:1,000), TOP3A (cat. no. 14525-1-AP, Proteintech, 1:500), DRP1 (cat. no. 611113, BD Biosciences, 1:1,000), PARP (cat. no. 9542, CST, 1:1,000), RAB7 (cat. no. 9367s, CST, 1:1,000) and VDAC1 (cat. no. ab15895, Abcam, 1:1,000).

Ratiometric flow cytometry to measure mitophagy flux

U2OS cells with stable expression of an mCherry–GFP–FIS1 tandem construct (a generous gift from Dr Ian Ganley's group[60]) were used to measure mitophagy via ratiometric flow cytometry as has been described previously[61]. Cells were transfected or treated with different mitophagy-inducing drugs 24 h before flow cytometry analysis on an Aria Fusion cell sorter using lasers set at 488 and 561 nm. Debris, dead cells and doublets were omitted via side/forward scatter profiling. A 'Tandem+' gate was set using unstained cells with the gate set to 1% 'tandem+'. FlowJo software (verson 10.8.0) was then used to analyse the mCherry/GFP ratio within the 'tandem+' gate. A 'mitophagy' gate was set based on the mCherry/GFP ratio of the bafilomycin A1-treated sample set to 5%.

Statistics and reproducibility

Microscopy data were quantified using Fiji (version 2.3.051, ImageJ, NIH). Wherever possible, data were quantified in a blinded fashion (accomplished using the blinded analysis plugin in Fiji). The mitochondria analyser plugin was used to quantify mitochondrial length[62]. All statistical analyses and graphs were generated using GraphPad Prism (version 9.5.1). Outliers were identified using the regression and outlier (ROUT) method. For most experiments, differences were compared using an unpaired, two-tailed Student's t-test. For some experiments, different populations of nucleoids (defined by size) within the same cell were compared by two-tailed, paired t-tests. The test used is denoted in the figure legends. No statistical method was used to pre-determine sample size.

Quantification of extramitochondrial nucleoids and overlap with cGAS/RAB7.

For FISH experiments, cells were selected for imaging if they displayed puncta positive for cGAS and DNA or mtDNA FISH. When imaging TFAM as a marker for released mtDNA in experiments with UL12.5 or HSV-1, cells with obviously reduced TFAM levels were selected for imaging. For all other experiments, cells with enlarged nucleoids were selected for imaging. For cells expressing RAB5A[S34N], we confirmed that the endosomal pathway was reduced (defined by less than 5 RAB5A puncta and less than 20 RAB7 puncta) in transfected cells before analysis. To quantify extramitochondrial nucleoids, the mitochondria channel was masked using automatic thresholding, and this mask was subtracted from the other channels using the image calculator in Fiji. Instances of overlap were then scored between the mtDNA FISH or TFAM and other channels (1 for overlap, 0 for no overlap) in a blinded fashion.

Quantification of nucleoid size and EdU intensity.

The DNA channel was thresholded (Otsu's method). A nuclear mask (generated by applying Gaussian blur with sigma radius of 4 to the Hoescht channel, followed by thresholding using Huang's method) was then subtracted from the DNA channel. Nucleoids within the remaining DNA signal were then measured using 'Analyze particles'. For experiments in MEFs, nucleoids were considered enlarged if larger than 0.4 µm^2 as described previously[7]. To quantify EdU intensity, EdU and DNA fluorescence intensity was measured within ROIs that were generated via 'Analyze

particles', which was applied to a binary image of mtDNA, which was generated using the 'AND' function in the image calculator by combining images of non-nuclear DNA and thresholded mitochondria (Li's method). To quantify the EdU/DNA ratio, the EdU intensity was divided by the DNA intensity and binned into 'normal' or 'enlarged' categories based upon the size of the nucleoid.

Quantification of mitochondria and ER-associated actin. The average nucleoid size in Airyscan images of control cells was first measured as described above, and nucleoids larger than 0.3 µm² were classified as enlarged. For each cell ($N = 5$), line scans (1.5 µm) were drawn through all enlarged nucleoids. As cells for these experiments were imaged at a higher zoom to minimize phototoxicity from performing four-colour Airyscan imaging on living cells, only a subset of the cell was imaged, and an average of three enlarged nucleoids were present per image (in total we measured 12 enlarged nucleoids across 5 TFAM-deficient clone 1 cells and 13 enlarged nucleoids across 5 TFAM-deficient clone 2 cells). An equivalent number of nucleoids <0.3 µm² were selected in a blinded fashion, for comparison (note also that there are fewer total nucleoids in TFAM-deficient cells[7]). The peak fluorescence intensity of each actin probe was measured and normalized to the mitochondrial or ER fluorescence intensity within 164 nm of the actin peak.

Quantification of overlap between mitochondria-localized enlarged nucleoids and RAB5. The average size of a nucleoid in mock infected cells imaged by spinning disk microscopy was measured as described above. This value (0.36 µm²) was used as a cutoff to identify enlarged nucleoids. Those that colocalized with mitochondria were scored for overlap with RAB5.

Quantification of overlap between mtDNA and ER. A binary image of the PicoGreen and mitochondria channels was generated using automatic thresholding (Otsu's method for PicoGreen and Li's method for mitochondria). A binary image of mitochondria-localized mtDNA was generated using the 'AND' function in the image calculator in Fiji using the binary PicoGreen and mitochondria channels, after which watershed was applied and ROIs greater than or equal to 100 nm² were identified using 'Analyze particles'. A binary image of the ER was generated using the auto local threshold in Fiji (Phansalkar method with radius of 100). The presence of the ER within each ROI was scored (1 for overlap and 0 for no overlap).

Quantification of LysoTracker Deep Red intensity with extramitochondrial mtDNA. A binary image of the Pico Green and mitochondria channels was generated using automatic thresholding (Otsu's method for Pico Green, Li's method for mitochondria). A binary image of non-mitochondrial Pico Green was generated by using image calculator to subtract mitochondria from Pico Green, after which watershed was applied and ROIs greater than or equal to 100 nm² were identified using 'Analyze particles'. ROIs were inspected and confirmed to be present outside of mitochondria in a blinded fashion. LysoTracker intensity was measured within these puncta, and background intensity (measured from bafilomycin A1-treated cells) was subtracted. Nucleoids with LysoTracker values greater than 0 were scored as positive.

Quantification of LC3 puncta. To identify LC3 puncta, a binary image of the LC3 channel was generated using automatic thresholding (Shanbhag's method), watershed applied and puncta >500 nm² were identified using 'Analyze particles'. LC3 intensity was measured within these puncta, and background intensity (measured from mock infected cells) was subtracted.

Reporting summary

Further information on research design is available in the Nature Portfolio Reporting Summary linked to this article.

Data availability

Source data are provided with this paper. All other data supporting the findings of this study are available from the corresponding author on reasonable request.

References

47. Woo, D. K. et al. Mitochondrial genome instability and ROS enhance intestinal tumorigenesis in APC(min/+) mice. *Am. J. Pathol.* **180**, 24–31 (2012).
48. Desai, P. & Person, S. Incorporation of the green fluorescent protein into the herpes simplex virus type 1 capsid. *J. Virol.* **72**, 7563–7568 (1998).
49. Etienne, L. et al. Visualization of herpes simplex virus type 1 virions using fluorescent colors. *J. Virol. Methods* **241**, 46–51 (2017).
50. Zhang, K. et al. Defective axonal transport of Rab7 GTPase results in dysregulated trophic signaling. *J. Neurosci.* **33**, 7451–7462 (2013).
51. Burel, A. et al. A targeted 3D EM and correlative microscopy method using SEM array tomography. *Development* **145**, dev160879 (2018).
52. Saalfeld, S., Fetter, R., Cardona, A. & Tomancak, P. Elastic volume reconstruction from series of ultra-thin microscopy sections. *Nat. Methods* **9**, 717–720 (2012).
53. Serra Lleti, J. M. et al. CLEMSite, a software for automated phenotypic screens using light microscopy and FIB–SEM. *J. Cell Biol.* **222**, e202209127 (2022).
54. Bogovic, J. A., Hanslovsky, P., Wong, A. & Saalfeld, S. Robust registration of calcium images by learned contrast synthesis. in *2016 IEEE 13th International Symposium on Biomedical Imaging (ISBI)* https://doi.org/10.1109/ISBI.2016.7493463 (IEEE, 2016).
55. Lee, C. T. et al. An open-source mesh generation platform for biophysical modeling using realistic cellular geometries. *Biophys. J.* **118**, 1003–1008 (2020).
56. Jorstad, A. et al. NeuroMorph: a toolset for the morphometric analysis and visualization of 3D models derived from electron microscopy image stacks. *Neuroinformatics* **13**, 83–92 (2015).
57. Schaffer, M. et al. Optimized cryo-focused ion beam sample preparation aimed at in situ structural studies of membrane proteins. *J. Struct. Biol.* **197**, 73–82 (2017).
58. Mastronarde, D. N. Automated electron microscope tomography using robust prediction of specimen movements. *J. Struct. Biol.* **152**, 36–51 (2005).
59. Kremer, J. R., Mastronarde, D. N. & McIntosh, J. R. Computer visualization of three-dimensional image data using IMOD. *J. Struct. Biol.* **116**, 71–76 (1996).
60. Allen, G. F. G., Toth, R., James, J. & Ganley, I. G. Loss of iron triggers PINK1/Parkin-independent mitophagy. *EMBO Rep.* **14**, 1127–1135 (2013).
61. Towers, C. G. et al. Mitochondrial-derived vesicles compensate for loss of LC3-mediated mitophagy. *Dev. Cell* **56**, 2029–42.e5 (2021).
62. Chaudhry, A., Shi, R. & Luciani, D. S. A pipeline for multidimensional confocal analysis of mitochondrial morphology, function, and dynamics in pancreatic β-cells. *Am. J. Physiol. Endocrinol. Metab.* **318**, E87–e101 (2020).
63. Ben-Hail, D. et al. Novel compounds targeting the mitochondrial protein VDAC1 inhibit apoptosis and protect against mitochondrial dysfunction. *J. Biol. Chem.* **291**, 24986–25003 (2016).

Author contributions

Competing interests

The authors declare no competing interests.

Additional information

Extended data is available for this paper at https://doi.org/10.1038/s41556-023-01343-1.
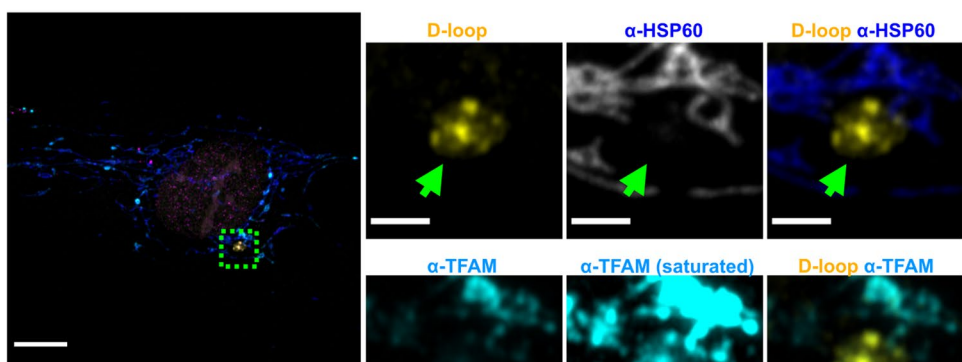
Supplementary information The online version contains supplementary material available at https://doi.org/10.1038/s41556-023-01343-1.

Correspondence and requests for materials should be addressed to Uri Manor or Gerald S. Shadel.
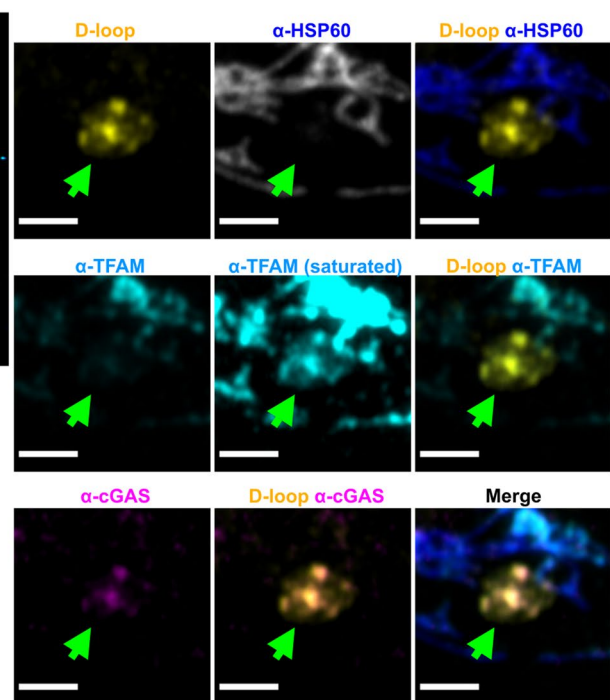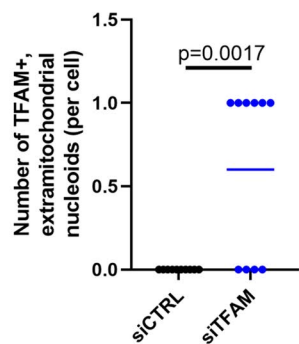
Peer review information *Nature Cell Biology* thanks the anonymous reviewers for their contribution to the peer review of this work. Peer reviewer reports are available.

Reprints and permissions information is available at www.nature.com/reprints.
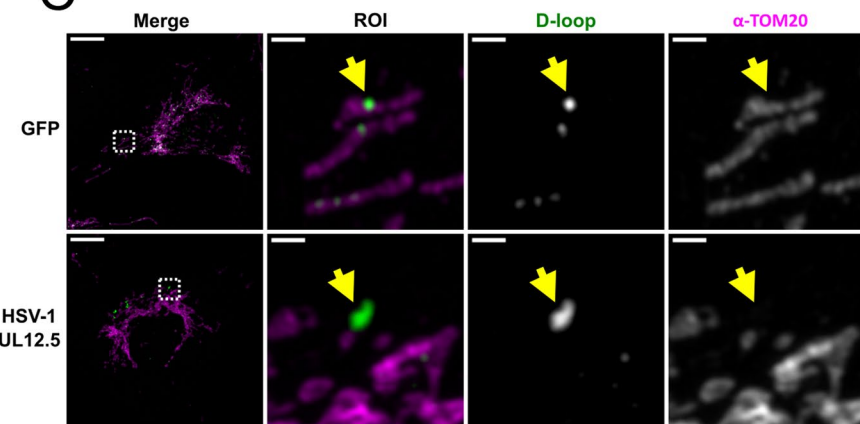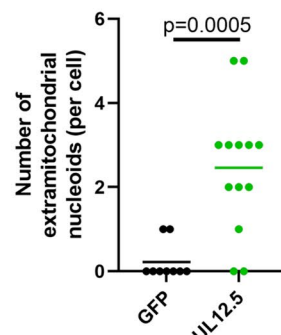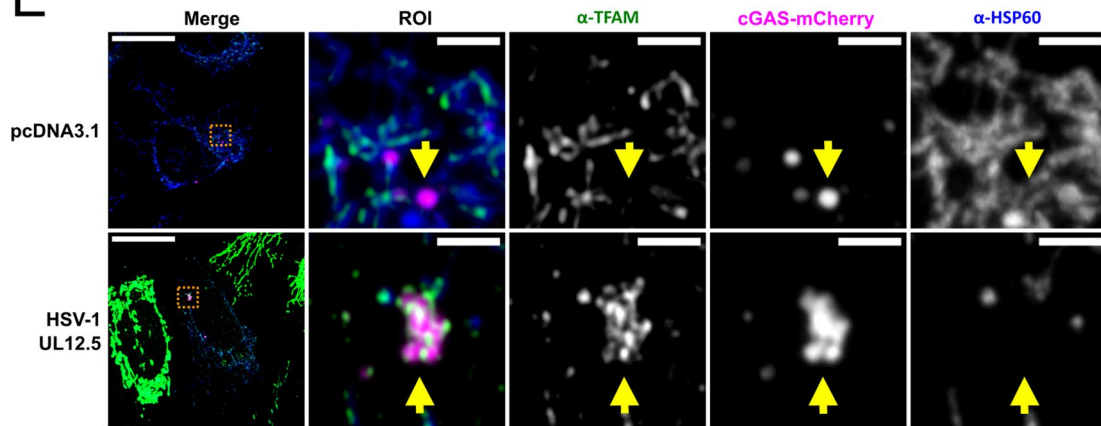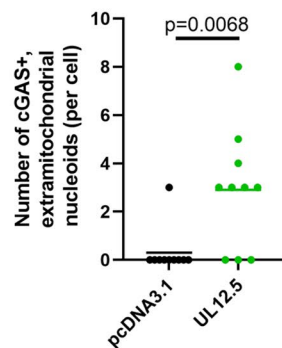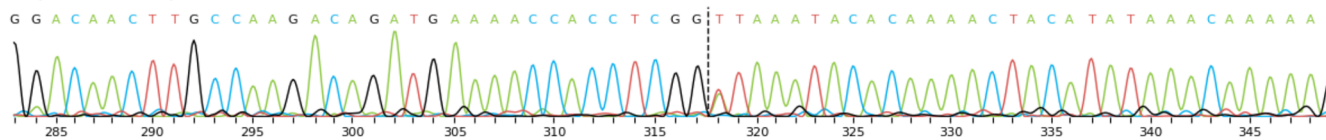
Extended Data Fig. 1 | See next page for caption.

Extended Data Fig. 1 | TFAM-bound nucleoids are present outside of mitochondria in TFAM knock-down and HSV-1 UL12.5-expressing cells. a) Airyscan imaging of mtDNA FISH using a D-loop probe, followed by immunofluorescence against cGAS, HSP60, and TFAM, in IMR-90 cells transfected TFAM siRNA. Scale bars = 10 μm for larger images, 2 μm for insets. **b)** Quantification of extramitochondrial nucleoids positive for TFAM. N = 10 cells for both conditions, and data were quantified from one representative experiment of three. siCTRL was compared to siTFAM (p = 0.0017). **c)** Airyscan imaging of mtDNA FISH (D-loop probe), followed by immunofluorescence against TOM20 in U2OS cells that were transfected with either HSV-1 UL12.5 or GFP (as a negative control). Scale bars = 10 μm, ROI scale bars = 1 μm. **d)** Quantification of nucleoids present outside of mitochondria. GFP was compared to UL12.5 (p = 0.0005). N = 9 cells for GFP, N = 13 cells for UL12.5, and data were quantified from one experiment of three. **e)** Airyscan imaging of TFAM and HSP60 immunofluorescence in U2OS cells transfected with cGAS-mCherry along with either pcDNA3.1 or HSV-1 UL12.5. For the cGAS-mCherry channel, image display settings were not held constant between pcDNA3.1 and UL12.5, to allow for visualization of cGAS-mCherry structures and accounting for differences in the level of exogenous expression. Similarly, image display settings of TFAM are not constant between pcDNA3.1 and UL12.5, to account for diminished TFAM levels caused by UL12.5 expression (also causing neighboring untransfected cells to appear saturated in the bottom image shown)[7]. Scale bars = 20 μm, inset scale bars = 2 μm. **f)** Quantification of extramitochondrial nucleoids, using TFAM as a marker for mtDNA and performed similarly to quantification in D. pcDNA3.1 was compared to UL12.5 (p = 0.0068). N = 10 cells for both conditions, and data were quantified from one representative experiment of three. All differences were compared using unpaired, two-tailed student's t test. For all plots, lines represent mean. Source numerical data are available in source data.
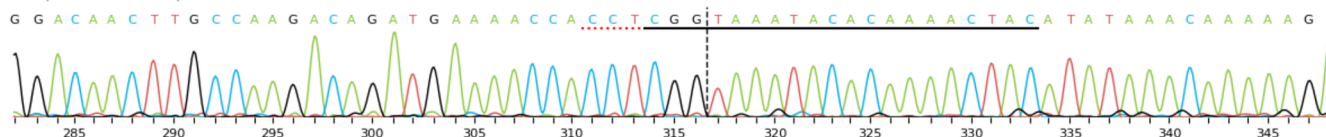
A
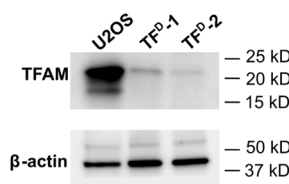
Edited Sample 283 to 348 bp

G G A C A A C T T G C C A A G A C A G A T G A A A A C C A C C T C G G T T A A A T A C A C A A A A C T A C A T A T A A A C A A A A
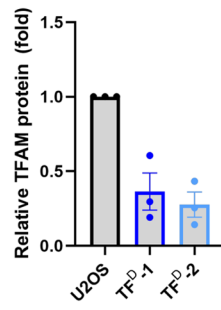
Control Sample 282 to 347 bp

G G A C A A C T T G C C A A G A C A G A T G A A A A C C A C C T C G G T A A A T A C A C A A A A C T A C A T A T A A A C A A A A A G

B

C

Relative TFAM protein (fold)

D

mtDNA abundance (%)
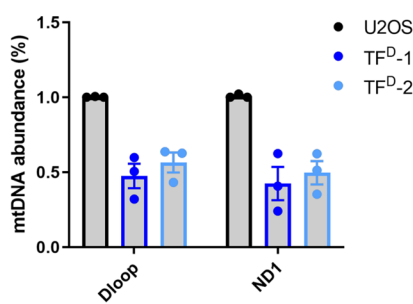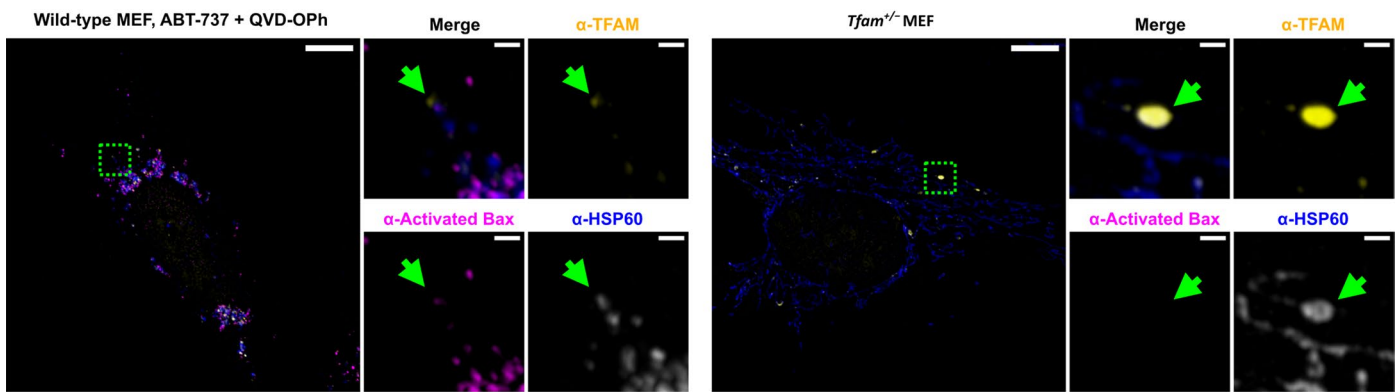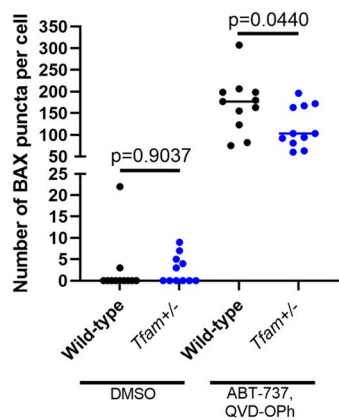
- U2OS
- TF^D-1
- TF^D-2

Extended Data Fig. 2 | Characterization of TFAM-deficient U2OS cells derived using CRISPR. a) Sequencing of U2OS TFAM-deficient clones, confirming insertion and frameshifting in exon 1 (top) relative to unedited U2OS cells (bottom). Similar results were obtained for both clones. **b)** Western blotting of TFAM and β actin (loading control) in two TFAM-deficient CRISPR clones (TF^D-1 and TF^D-2) as well as the parental U2OS cells. **c)** Quantification of B. Dots represent replicates of independent experiments (N = 3). **d)** mtDNA abundance (relative mtDNA copy number) analyzed by qPCR with D-loop and ND1 primers, normalized to nuclear 18 S. Dots represent replicates (N = 3). All data are reported as mean ± SEM. Source numerical data and unprocessed blots are available in source data.
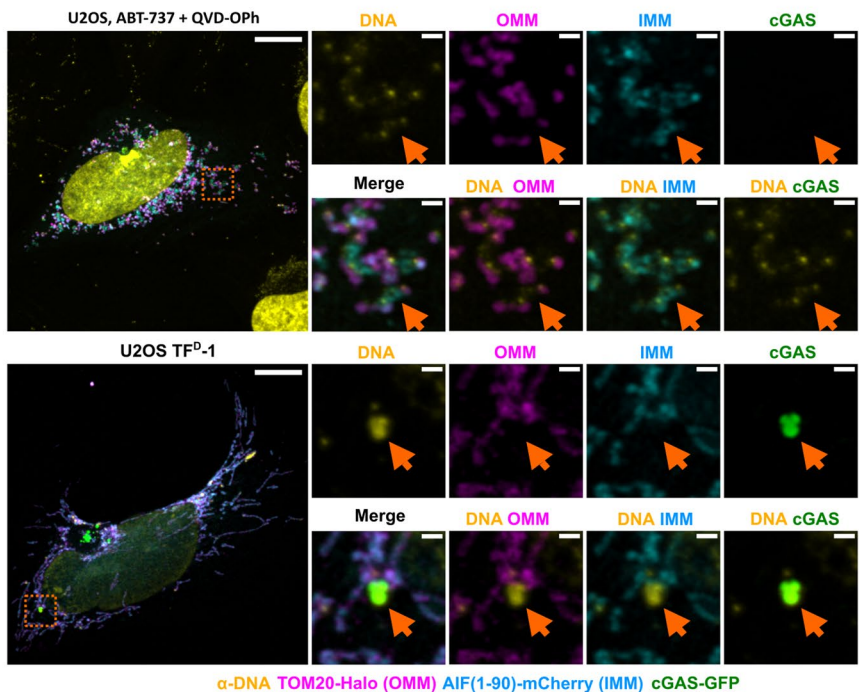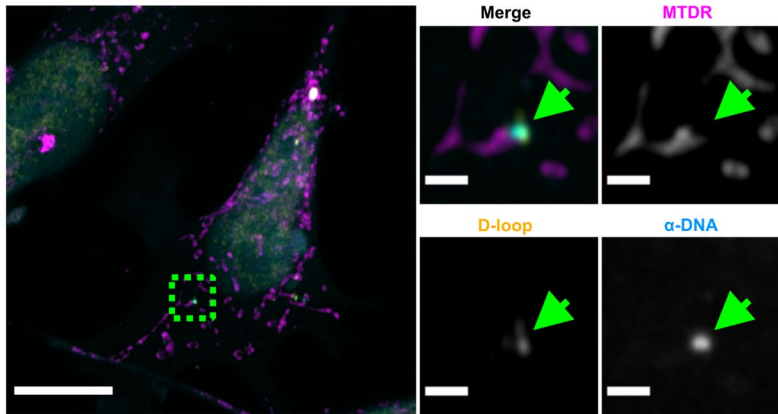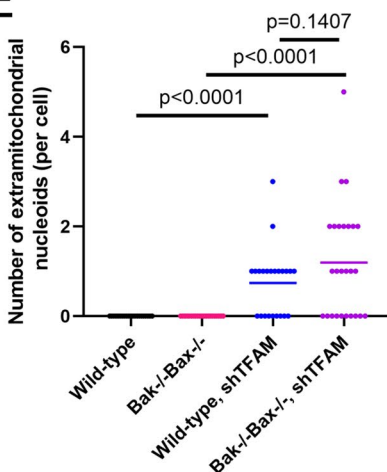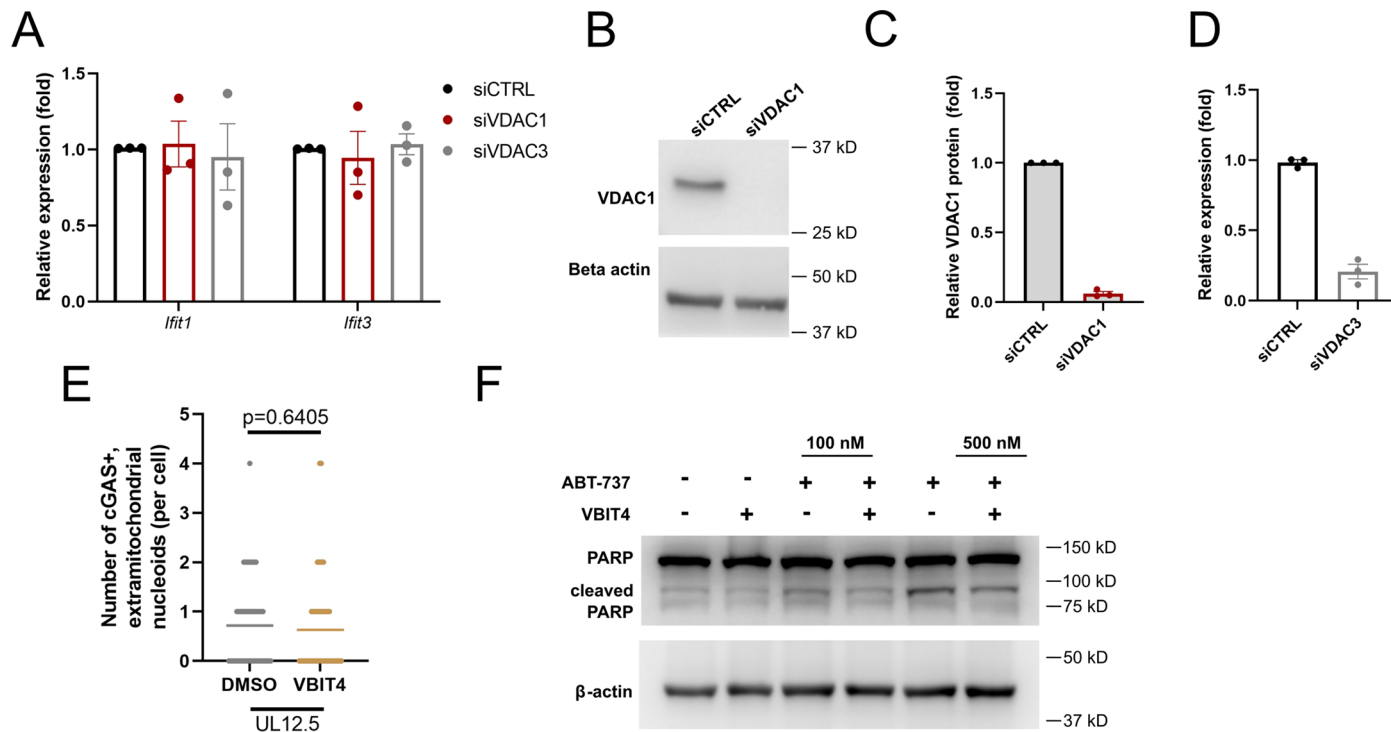
Extended Data Fig. 3 | See next page for caption.
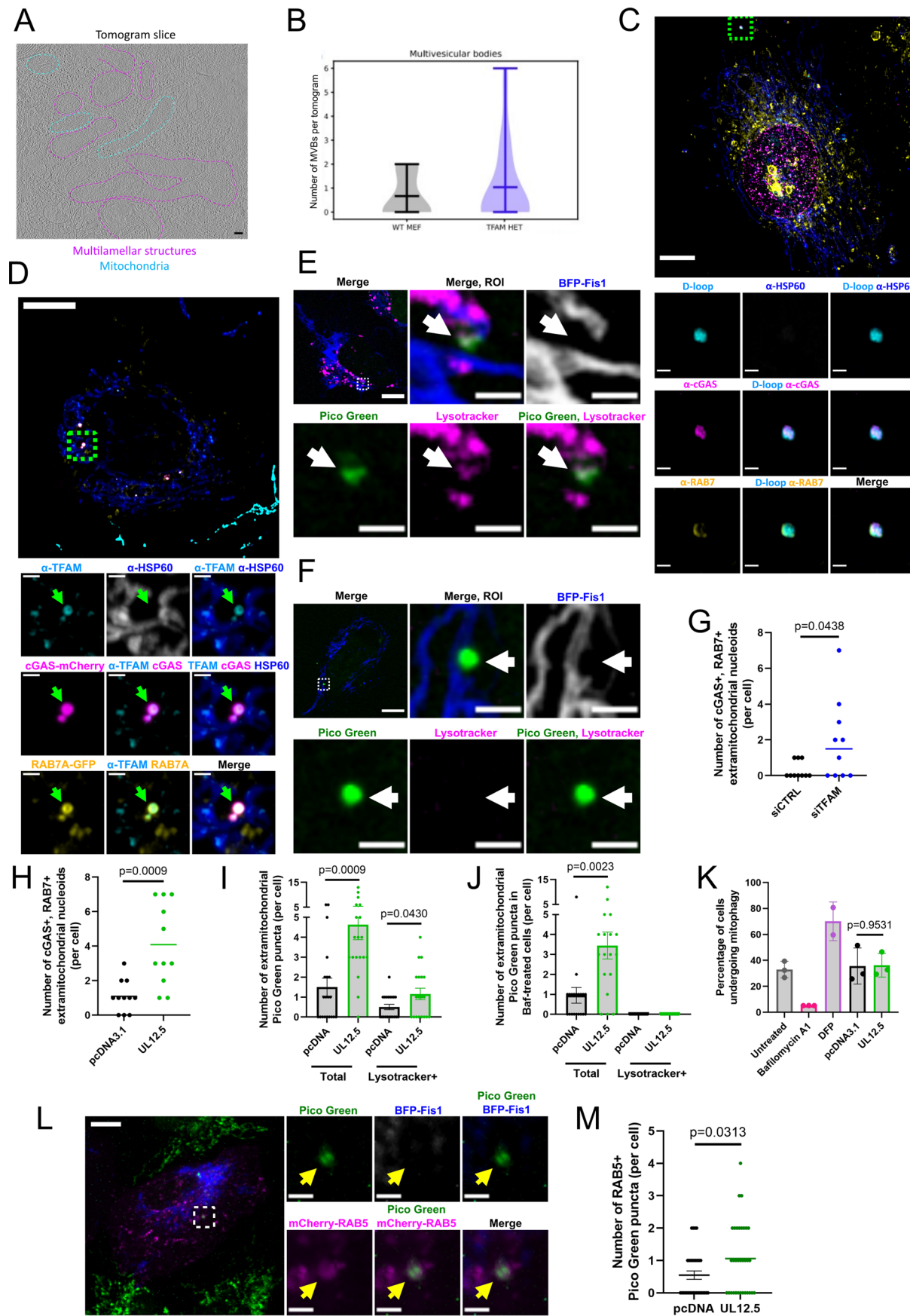
Extended Data Fig. 3 | Enlarged nucleoids are not released through BAX pores. a) Airyscan imaging of immunofluorescence against activated BAX alongside TFAM and HSP60 in primary wild type and *Tfam*+/− MEFs. As a positive control, BAX-mediated mtDNA release was induced by treatment with ABT-737 (10 μM) plus QVD-OPh (20 μM) for 4 hours. Image display settings are held constant for BAX but not for TFAM or HSP60 to account for differences in the expression of each between experimental conditions. **b)** Quantification of **(A)**. The number of BAX puncta per cell was counted. Wild-type was compared to *Tfam*+/− (DMSO: p = 0.9037, ABT-737/QVD-OPh: p = 0.0440). N = 11 cells for each condition. Data were quantified from one representative experiment of three. **c)** Airyscan imaging of TFAM-deficient U2OS cells expressing AIF(1-90)-mCherry (IMM, inner mitochondrial membrane), TOM20-Halo (OMM, outer mitochondrial membrane), and cGAS-GFP, along with immunofluorescence against DNA. ABT-737 and QVD-OPh treatment was used as a positive control for IMM herniation beyond the OMM. Image display settings are not the same between experimental conditions due to differences in exogenous expression as well as intensity of mtDNA puncta. Results were reproducible across three independent experiments. **d)** Airyscan imaging of mtDNA FISH using a D-loop probe in *Bak*−/−*Bax*−/− MEFs stably expressing TFAM shRNA and labeled with Mitotracker Deep Red (MTDR). Results are representative of three independent experiments. **e)** Quantification of extramitochondrial nucleoids per cell. Wild-type was compared to wild-type shTFAM (p < 0.0001), *Bak*−/−*Bax*−/− was compared to *Bak*−/−*Bax*−/− shTFAM (p < 0.0001), and wild-type shTFAM was compared to *Bak*−/−*Bax*−/− shTFAM (p = 0.1407). N = 21 cells for both wild type and *Bak*−/−*Bax*−/− MEFs, N = 23 cells for WT shTFAM, N = 26 cells for *Bak*−/−*Bax*−/− shTFAM, and data were quantified from one representative experiment of three. For all panels, scale bars = 10 μm and inset scale bars = 1 μm. For all plots, line represents mean. All differences were compared using unpaired, two-tailed student's t test. Source numerical data are available in source data.

Extended Data Fig. 4 | Enlarged nucleoids are not released through VDAC pores. a) qRT-PCR of primary *Tfam*^{+/−} MEFs transfected with control, VDAC1, or VDAC3 siRNAs, normalized to β actin. Dots represent biological replicates of independent experiments (N = 3). **b)** Western blotting of VDAC1 and β actin (loading control) in primary MEFs transfected with control or VDAC1 siRNAs. **c)** Quantification of B. Dots represent biological replicates (N = 3). **d)** qRT-PCR of *Vdac3* in primary *Tfam*^{+/−} MEFs transfected with control or VDAC3 siRNAs, normalized to β actin. qPCR data is shown due to the fact that attempts to blot for VDAC3 failed. Dots represent biological replicates of independent experiments (N = 3). **e)** U2OS cells expressing HSV-1 UL12.5 and cGAS-Halo were treated with either DMSO or VBIT4 (10 μM) for 24 hrs and imaged for TFAM and HSP60 immunofluorescence using resonance scanning confocal microscopy.

The number of extramitochondrial cGAS+ TFAM+ puncta was scored, and DMSO was compared to VBIT4 by unpaired, two-tailed t test (p = 0.6405). N = 50 cells for DMSO and N = 49 cells for VBIT4, and data were quantified from three independent experiments. **f)** Western blotting against PARP in cells treated with the indicated concentration (100 nM or 500 nM) of the apoptosis inducer ABT-737 along with either DMSO or VBIT4 (10 μM). The reduction of cleaved PARP indicates that the induction of apoptosis is reduced in cells treated with VBIT4, as previously published[63], demonstrating that the VBIT4 used in panel E is active. β actin was probed as a loading control. Results were reproduced across three independent experiments. For all plots, data are reported as mean ± SEM. Source numerical data and unprocessed blots are available in source data.
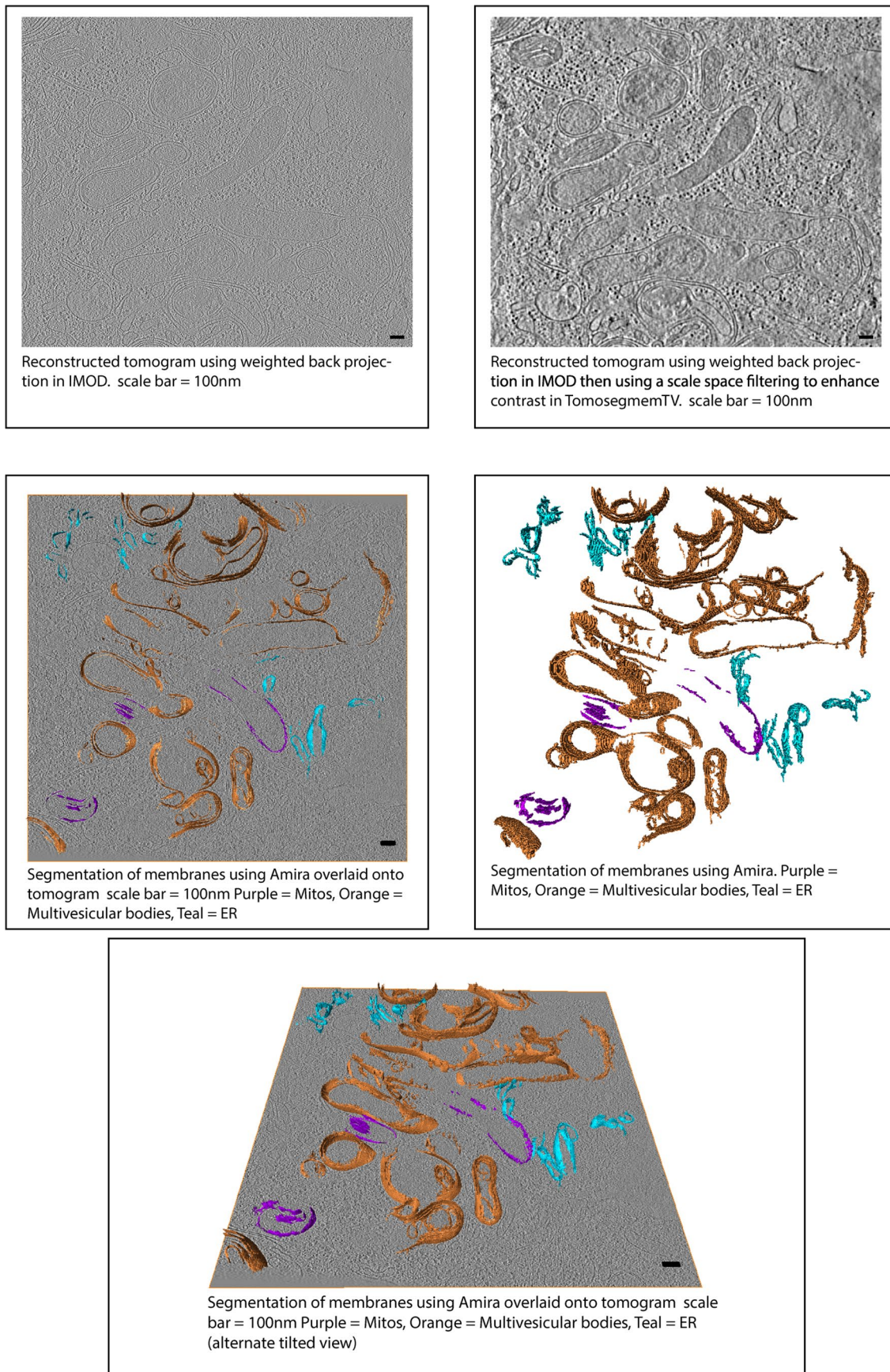
**Extended Data Fig. 5 | See next page for caption.**
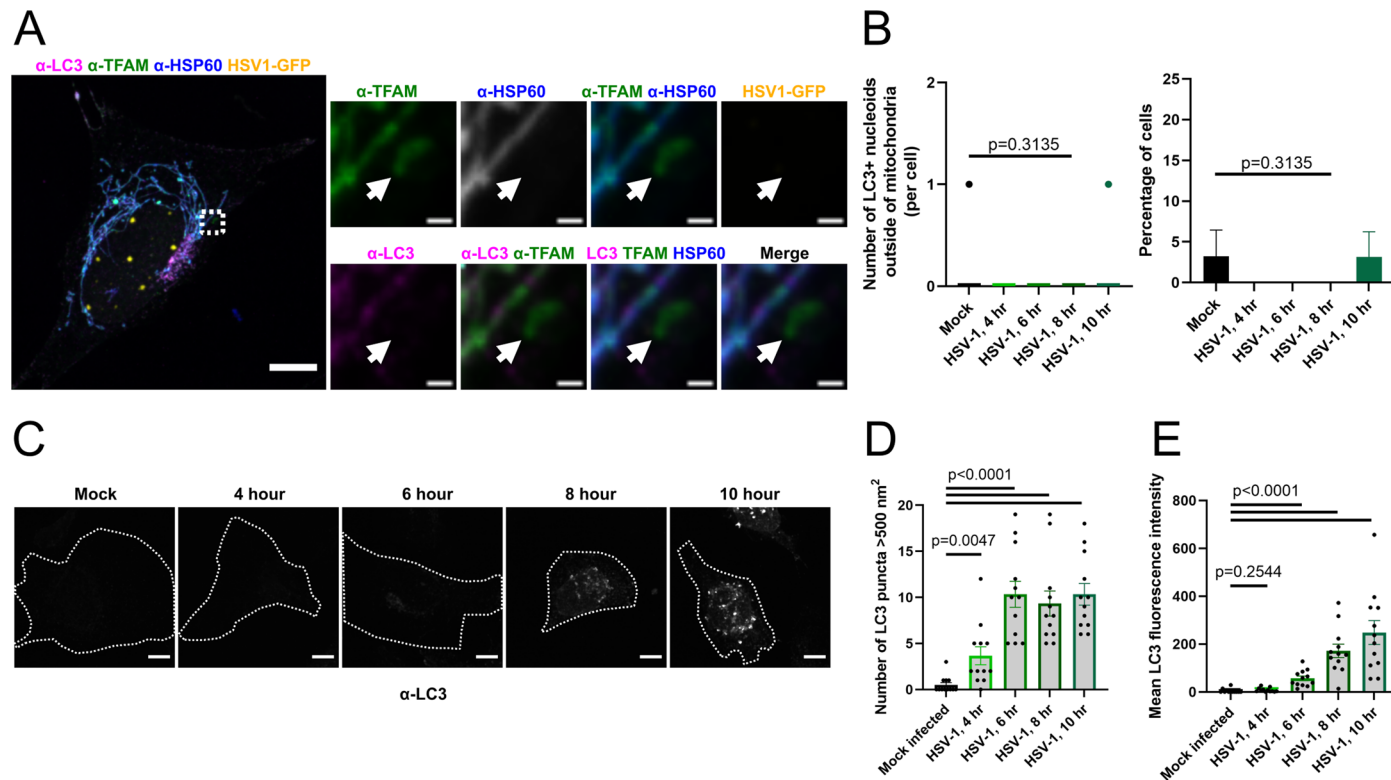
Extended Data Fig. 5 | Enlarged nucleoids traffic through endosomes.
a) A representative tomogram slice (of 27) of a *Tfam*$^{+/-}$ MEF cell imaged by cellular cryo-electron tomography. Multivesicular bodies are highlighted by dashed pink lines, and mitochondria are highlighted by dashed cyan lines. Scale bar = 100 nm. **b)** The presence of multivesicular bodies was scored as described under methods. N = 15 tomograms (fields of view) for wild-type MEFs and N = 27 tomograms (fields of view) for *Tfam*$^{+/-}$ MEFs. Data are reported as mean ± SD. **c)** Airyscan imaging of mtDNA FISH (D-loop probe), followed by immunofluorescence against RAB7, cGAS, and HSP60 in TFAM-depleted IMR-90 cells. Scale bars = 10 μm and inset scale bars = 1 μm. Results are representative of three independent experiments. **d)** Airyscan imaging of TFAM and HSP60 immunofluorescence in U2OS cells expressing RAB7A-GFP, cGAS-mCherry, and HSV-1 UL12.5. Scale bars = 10 μm and inset scale bars = 1 μm. Results are representative of three independent experiments. **e)** Confocal imaging of live U2OS cells transfected with BFP-Fis1 (mitochondrial OMM) and UL12.5 and labeled with Pico Green and Lysotracker Deep Red. **f)** Same as panel E but treated with bafilomycin A1 (which prevents lysosomal acidification, 200 nM) immediately prior to Lysotracker labeling (15 min.) and additionally for the duration of Lyosotracker labeling and imaging. Scale bars = 10 μm and inset scale bars = 2 μm. For panels E and F, the experiment was performed three times with similar results. **g)** Quantification of panel C. The number of extramitochondrial nucleoids per cell that were positive for both cGAS and RAB7 was scored for cells transfected with control or TFAM siRNAs. siCTRL was compared to siTFAM (p = 0.0428). N = 10 cells for each condition, and data were quantified from one representative experiment of three. **h)** Quantification of panel D. The number of TFAM-marked nucleoids per cell that were positive for both cGAS and RAB7 was scored, and pcDNA3.1 was compared to UL12.5 (p = 0.0009). N = 11 cells for

both conditions, and data were quantified from one representative experiment of three. **i)** Quantification of panel E. The number of extramitochondrial Pico Green puncta were scored, and pcDNA3.1 was compared to UL12.5 (p = 0.0009). Lysotracker+ puncta were identified by measuring Lysotracker intensity within these Pico Green puncta. Values above background intensities (measured in bafilomycin-treated cells) were counted as positive, and pcDNA3.1 was compared to UL12.5 (p = 0.043). **j)** Quantification of panel F. Extramitochondrial Pico Green puncta in bafilomycin-treated cells were scored and pcDNA3.1 was compared to UL12.5 (p = 0.0023) (no Lysotracker+ Pico Green puncta were observed in bafilomycin-treated cells). For panels I and J, N = 20 cells for pcDNA3.1 and N = 19 cells for UL12.5; data were pooled from two independent experiments; and the experiment was repeated a third time with similar results. **k)** Quantification of mitophagy via ratiometric flow cytometry performed in U2OS cells with stable expression of mCherry-GFP-Fis1. Cells were either transfected with pcDNA3.1, UL12.5 or treated with Bafilomycin-A1 (20 nM) or Deferiprone (DFP 1 mM) 24 hours before flow cytometry analysis. The data are shown as the average ratio of mCherry/GFP ± SEM from biological replicate experiments shown as dots (N of 2-3). pcDNA3.1 was compared to UL12.5 (p = 0.9531). **l)** Spinning disk imaging of Pico Green (DNA), BFP-Fis1 (mitochondria), and mCherry-RAB5B (early endosomes) in live cells expressing HSV-1 UL12.5. Scale bars = 10 μm and inset scale bars = 2 μm. This experiment was performed three times with similar results. **m)** Quantification of extramitochondrial Pico Green puncta also positive for mCherry-RAB5B. pcDNA3.1 was compared to UL12.5 (p = 0.0313). N = 31 cells for pcDNA3.1, N = 34 cells for UL12.5, and data were quantified from one representative experiment of three. For all plots, line represents mean, and all graphs represent mean ± SEM. All differences were compared using unpaired, two-tailed student's t test. Source numerical data are available in source data.

Reconstructed tomogram using weighted back projection in IMOD. scale bar = 100nm

Reconstructed tomogram using weighted back projection in IMOD then using a scale space filtering to enhance contrast in TomosegmemTV. scale bar = 100nm

Segmentation of membranes using Amira overlaid onto tomogram scale bar = 100nm Purple = Mitos, Orange = Multivesicular bodies, Teal = ER

Segmentation of membranes using Amira. Purple = Mitos, Orange = Multivesicular bodies, Teal = ER

Segmentation of membranes using Amira overlaid onto tomogram scale bar = 100nm Purple = Mitos, Orange = Multivesicular bodies, Teal = ER (alternate tilted view)
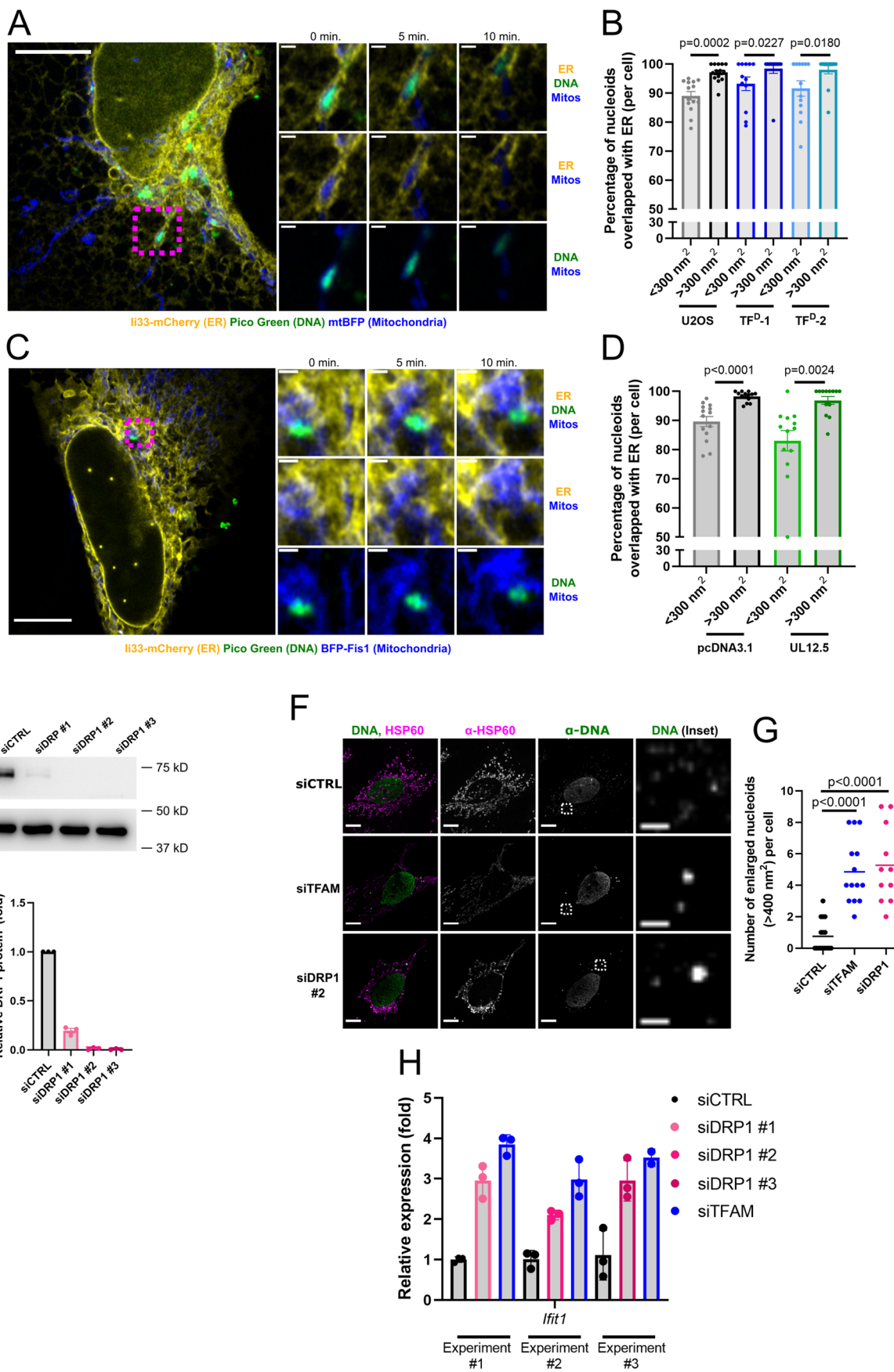
Extended Data Fig. 6 | Segmentation of organelles in cryo-EM tomograms of *Tfam*^{+/−} MEFs. A representative tomogram slice (of a total of 27) of a *Tfam*^{+/−} MEF cell imaged by cellular cryo-electron tomography. Membranes were segmented and colored orange for multivesicular bodies, purple for mitochondria, and teal for ER. Scale bar = 100 nm.

Extended Data Fig. 7 | HSV1 does not trigger re-localization of enlarged nucleoids into autophagosomes. a) Spinning disk imaging of LC3, TFAM, and HSP60 immunofluorescence in a U2OS cell 8 hours after infection with HSV1-GFP. Larger scale bar = 10 µm and inset scale bars = 1 µm. This experiment was performed three times with similar results. **b)** The number of non-mitochondrial TFAM puncta that overlapped with LC3 was scored. Mock infected cells were compared to cells infected for 8 hours (p = 0.3135). Number of cells: N = 31 for mock, N = 33 for 4 hr, N = 31 for 6 hr, N = 32 for 8 and 10 hr, and data were pooled from three independent experiments. The same dataset was used to generate both graphs. **c)** Spinning disk imaging of LC3 immunofluorescence in U2OS cells infected with HSV1-GFP and fixed at the indicated timepoints after

infection. Scale bars = 10 µm. This experiment was performed three times with similar results. **d)** The number of LC3 puncta per cell was scored and compared between mock and infected cells (p = 0.0047 for 4 hr, p < 0.0001 for 6, 8, and 10 hr). **e)** The mean fluorescence intensity within LC3 puncta was measured (see Methods) and compared between mock and infected cells (p = 0.2544 for 4 hr, p < 0.0001 for 6, 8, and 10 hr). For panels D and E, N = 12 cells per condition, and data were quantified from one representative experiment of three. For all plots, line represents mean, and all graphs represent mean ± SEM. All differences were compared using unpaired, two-tailed student's t test. Source numerical data are available in source data.
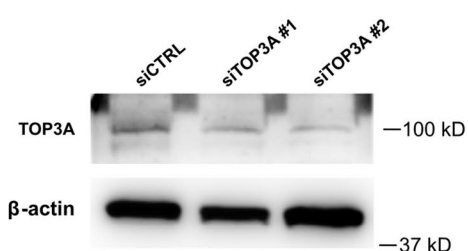
Extended Data Fig. 8 | See next page for caption.
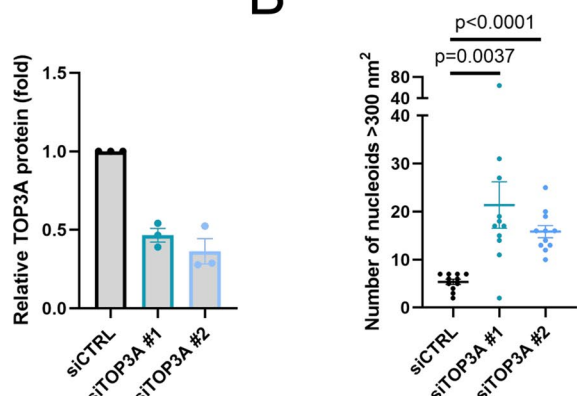
Extended Data Fig. 8 | Nucleoids cluster at mitochondria/ER contacts and are associated with reduced mitochondrial fission. a) Airyscan imaging of a live TFAM-deficient U2OS cell (TF^D-2) labeled with Ii33-mCherry (ER), Pico Green (DNA), and mtBFP (mitochondria). Time-lapse imaging demonstrates that mitochondria/ER forms contacts around enlarged nucleoids. This experiment was performed three times with similar results. **b)** Overlap between the ER and mitochondria-localized nucleoids was scored (see Methods). Enlarged nucleoids (>300 nm^2) were compared to normal-sized nucleoids (<300 nm^2) within the same cells using two-tailed, paired t tests (p = 0.0002 for U2OS, p = 0.0227 for TF^D-1, p = 0.0180 for TF^D-2). Number of cells: N = 14 for U2OS, N = 12 for TF^D-1, N = 13 for TF^D-2, and data were pooled from three experiments. **c)** The same experiment in panel A was repeated in cells expressing UL12.5. For panels A and D, scale bars = 10 μm and inset scale bars = 1 μm. This experiment was performed three times with similar results. **d)** Mitochondria/ER contacts at nucleoids were quantified as in Panel B. Enlarged nucleoids (>300 nm^2) were compared to normal-sized nucleoids (<300 nm^2) within the same cells using two-tailed, paired t tests (p < 0.0001 for pcDNA3.1, p = 0.0024 for UL12.5). N = 14 cells for pcDNA3.1, N = 13 cells for UL12.5, and data were pooled from three experiments. For panels B and D, data are reported as mean ± SEM. **e)** Western blotting of DRP1 and β actin (loading control) in primary MEFs transfected with control or DRP1 siRNAs. Quantification is shown on the right, and dots represent biological replicates of independent experiments (N = 3). **f)** Confocal imaging of primary wild-type MEFs transfected with siRNAs against TFAM or DRP1. Immunofluorescence against DNA and HSP60 is shown. Scale bars = 10 μm and inset scale bars = 2 μm. This experiment was performed three times with similar results. **g)** Quantification of nucleoids in panel F. The number of nucleoids per cell larger than 0.4 um^2 was quantified by thresholding the non-nuclear DNA signal and measuring particle size using ImageJ. siCTRL was compared to siTFAM or siDRP1 using unpaired, two-tailed student's t test (p < 0.0001). N = 16 cells for siCTRL, N = 14 cells for siTFAM, and N = 11 cells for siDRP1. Data were quantified from one representative experiment of three. Line represents mean. **h)** qRT-PCR of interferon-stimulated genes (ISGs, normalized to β actin) in primary wild-type MEFs transfected with control, TFAM, or one of three independent DRP1 siRNAs. Three independent, representative experiments performed on different days are combined onto one graph for ease of visualization. Dots represent technical replicates, and data are reported as mean ± standard deviation. Source numerical data and unprocessed blots are available in source data.
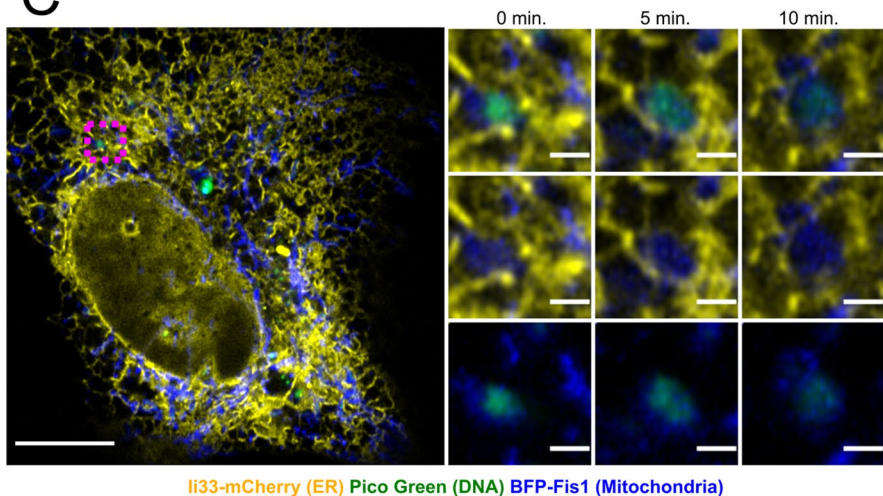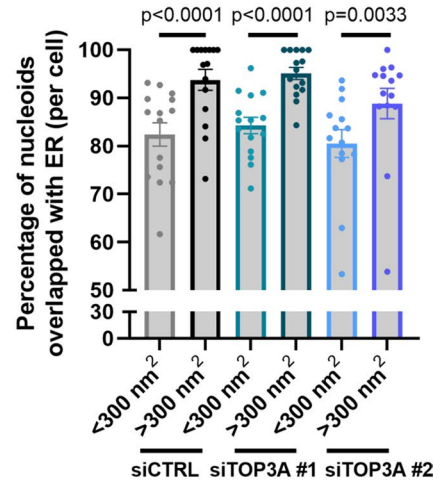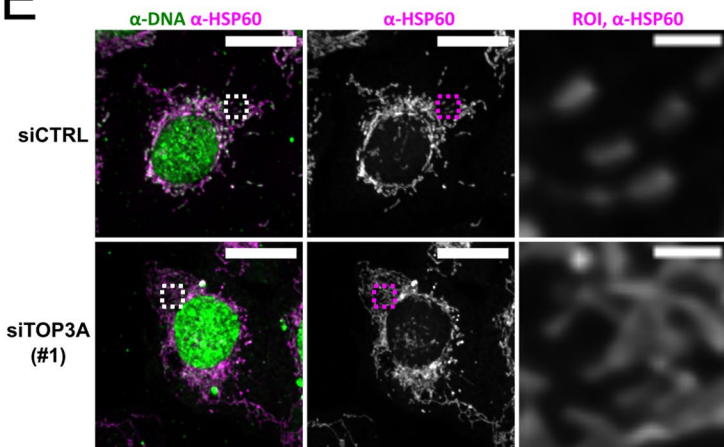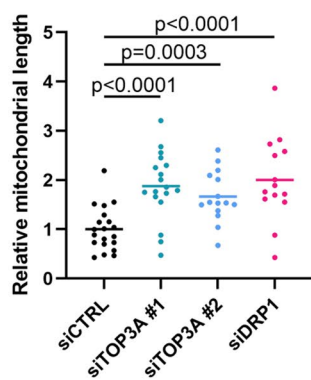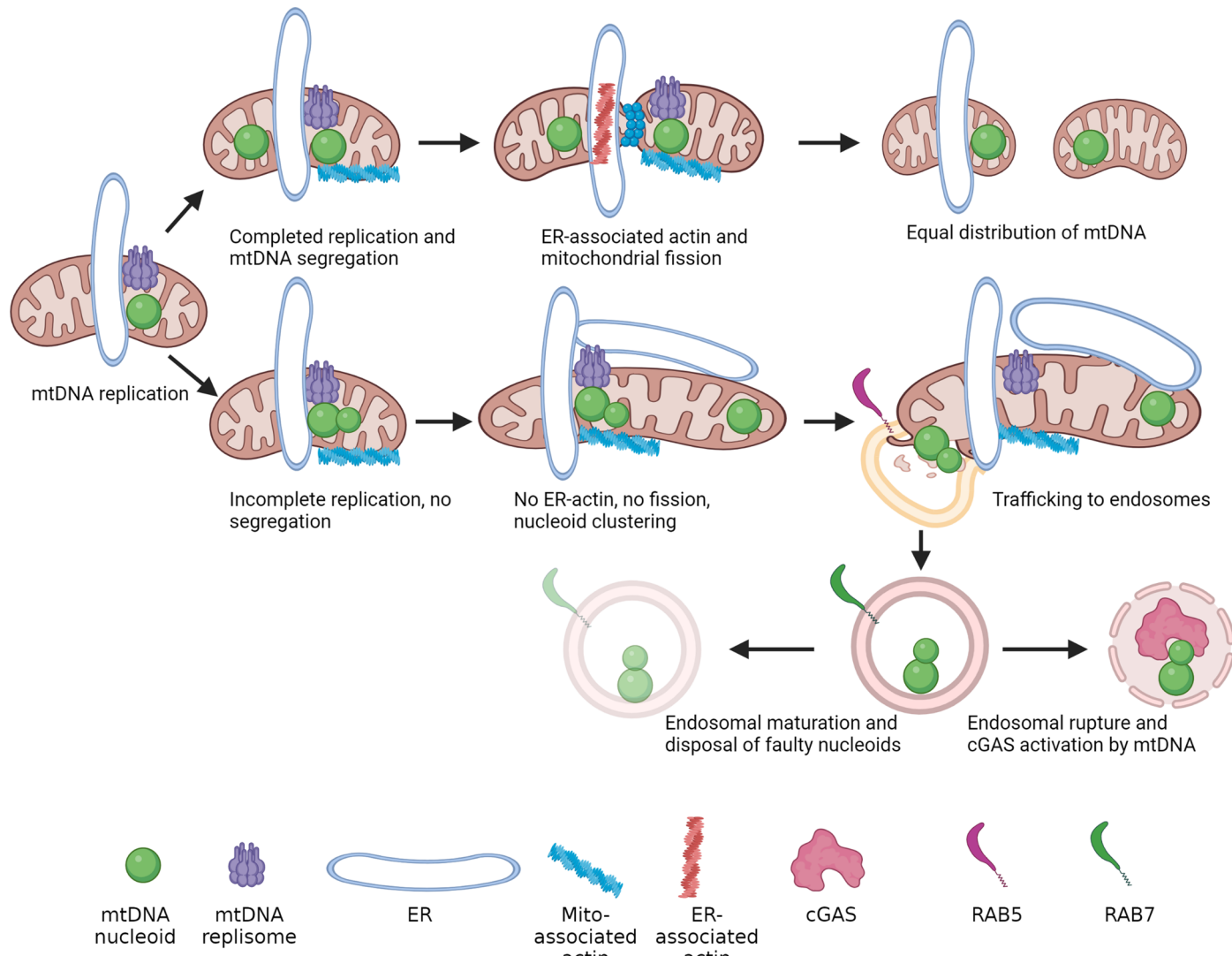
Extended Data Fig. 9 | See next page for caption.

Extended Data Fig. 9 | Loss of mtDNA segregation causes the formation of enlarged nucleoids at mitochondria/ER contact sites and elongates mitochondria. a) Western blotting of TOP3A and β actin (loading control) in U2OS cells transfected with control or TOP3A siRNAs. Quantification of western blot data is shown in the graph (right), dots represent replicates of independent experiments (N = 3). **b)** The number of nucleoids larger than 300 nm^2 was scored (using confocal images shown in Fig. 8a). siCTRL was compared to siTOP3A siRNAs by unpaired, two-tailed t test (p = 0.0037 for siRNA #1, p < 0.0001 for siRNA #2). N = 11 cells per condition, and data were quantified from one representative experiment of three. **c)** Airyscan imaging of Ii33-mCherry (ER), Pico Green (DNA), and BFP-Fis1 (mitochondria) of live cells depleted of TOP3A by siRNA (#2). Time-lapse imaging demonstrates mitochondria/ER contacts around enlarged nucleoids. Scale bars = 10 µm and inset scale bars = 1 µm. This experiment was performed three times with similar results. **d)** Overlap between the ER and mitochondria-localized nucleoids was scored (see Methods).

Enlarged nucleoids (>300 nm^2) were compared to normal-sized nucleoids (<300 nm^2) within the same cells using two-tailed, paired t tests (p < 0.0001 for siCTRL, p < 0.001 for siTOP3A #1, p = 0.0033 for siTOP3A #2). N = 15 cells for siCTRL and siTOP3A #1, N = 14 cells for siTOP3A #2, and data were pooled from three experiments. **e)** Spinning disk imaging of U2OS cells transfected with the indicated siRNAs, followed by immunofluorescence against DNA and HSP60. Scale bars = 20 µm and inset scale bars = 2 µm. This experiment was performed three times with similar results. **f)** Quantification of F (see Methods). siCTRL was compared to siRNAs against TOP3A and DRP1 using unpaired, two-tailed t test (p < 0.0001 for siTOP3A #1, p = 0.0003 for siTOP3A #2, p < 0.0001 for siDRP1). Number of cells: N = 20 for siCTRL, N = 18 for siTOP3A #1, N = 15 for siTOP3A #2, N = 14 for siDRP1. Data were quantified from one representative experiment of three. For all graphs, data are reported as mean ± SEM. Source numerical data and unprocessed blots are available in source data.

Extended Data Fig. 10 | Model summarizing endosome-mediated disposal of dysfunctional nucleoids. Following mtDNA replication, a signal is sent from mitochondria to the ER allowing for polymerization of ER-associated actin, which allows newly replicated nucleoids to segregate via mitochondrial fission. If problems arise during mtDNA replication or segregation as a result of mtDNA damage, no signal is sent to the ER, and actin does not associate with the ER. If nucleoids are unable to properly segregate through mitochondrial fission, a fission checkpoint is enacted (to wait for the completion of mtDNA segregation), and nucleoids accumulate at sites of replication. If not rectified, the dysfunctional nucleoids are trafficked to endosomes and are ultimately degraded by trafficking through late endosomes. However, a subset of late endosomes fails to fully mature and ultimately rupture, enabling cGAS to bind to mtDNA and trigger innate immune signalling.

nature portfolio

Corresponding author(s):   Uri Manor and Gerald Shadel

Last updated by author(s):   Dec 19, 2023

Reporting Summary

Nature Portfolio wishes to improve the reproducibility of the work that we publish. This form provides structure for consistency and transparency in reporting. For further information on Nature Portfolio policies, see our Editorial Policies and the Editorial Policy Checklist.

Statistics

For all statistical analyses, confirm that the following items are present in the figure legend, table legend, main text, or Methods section.

n/a	Confirmed	
☐	☒	The exact sample size (*n*) for each experimental group/condition, given as a discrete number and unit of measurement
☐	☒	A statement on whether measurements were taken from distinct samples or whether the same sample was measured repeatedly
☐	☒	The statistical test(s) used AND whether they are one- or two-sided *Only common tests should be described solely by name; describe more complex techniques in the Methods section.*
☒	☐	A description of all covariates tested
☒	☐	A description of any assumptions or corrections, such as tests of normality and adjustment for multiple comparisons
☐	☒	A full description of the statistical parameters including central tendency (e.g. means) or other basic estimates (e.g. regression coefficient) AND variation (e.g. standard deviation) or associated estimates of uncertainty (e.g. confidence intervals)
☐	☒	For null hypothesis testing, the test statistic (e.g. *F*, *t*, *r*) with confidence intervals, effect sizes, degrees of freedom and *P* value noted *Give P values as exact values whenever suitable.*
☒	☐	For Bayesian analysis, information on the choice of priors and Markov chain Monte Carlo settings
☒	☐	For hierarchical and complex designs, identification of the appropriate level for tests and full reporting of outcomes
☒	☐	Estimates of effect sizes (e.g. Cohen's *d*, Pearson's *r*), indicating how they were calculated

Our web collection on statistics for biologists contains articles on many of the points above.

Software and code

Policy information about availability of computer code

Data collection	Zeiss LSM 880 Airyscan confocal system, Zeiss spinning disk confocal system, Olympus FV3000 confocal system, Leica SP5 confocal system
Data analysis	Images were airyscan processed using the auto-filter 3D settings in Zen Black (Zeiss, version 2.3). All images were processed and analyzed using Fiji (version 2.3.051). All statistical analysis was performed using Graphpad Prism (version 9.5.1). Imaris (version 9.9) was used to align and visualize 3D-SEM data. Blender (version 2.79) was used to visualize FIB-SEM data. Flow cytometry data was analyzed using FlowJo (verson 10.8.0).

For manuscripts utilizing custom algorithms or software that are central to the research but not yet described in published literature, software must be made available to editors and reviewers. We strongly encourage code deposition in a community repository (e.g. GitHub). See the Nature Portfolio guidelines for submitting code & software for further information.

Data

Policy information about availability of data

All manuscripts must include a data availability statement. This statement should provide the following information, where applicable:
- Accession codes, unique identifiers, or web links for publicly available datasets
- A description of any restrictions on data availability
- For clinical datasets or third party data, please ensure that the statement adheres to our policy

All data are provided with the paper, and any raw data will be provided by the corresponding authors upon reasonable request, as stated in the manuscript.

Field-specific reporting

Please select the one below that is the best fit for your research. If you are not sure, read the appropriate sections before making your selection.

☒ Life sciences   ☐ Behavioural & social sciences   ☐ Ecological, evolutionary & environmental sciences

For a reference copy of the document with all sections, see nature.com/documents/nr-reporting-summary-flat.pdf

Life sciences study design

All studies must disclose on these points even when the disclosure is negative.

Sample size	For imaging experiments, at least ten cells per experimental condition were analyzed per experiment. Ten cells were imaged per condition per experiment using airyscan microscopy, and 15-30 cells were imaged per condition per experiment for all other types of microscopy. No statistical test was used to determine sample size. For qPCR experiments to analyze interferon-stimulated gene expression, at least three biological replicates were performed, and three technical replicates were performed for each biological replicate. The sample sizes used produced statistically significant results.
Data exclusions	For qPCR experiments, a Cq value was excluded if the difference from the other two replicates was more than 0.5. Any outliers were identified using the ROUT method in Graphpad Prism prior to exclusion. No other data was excluded.
Replication	All experiments were replicated at least twice. All attempts at replication were successful.
Randomization	Randomization is not relevant in this study as all experiments were performed using the same experimental conditions.
Blinding	Blinding was not conducted as all results are inherently objective and quantitatively measured.

Reporting for specific materials, systems and methods

We require information from authors about some types of materials, experimental systems and methods used in many studies. Here, indicate whether each material, system or method listed is relevant to your study. If you are not sure if a list item applies to your research, read the appropriate section before selecting a response.

Materials & experimental systems

n/a	Involved in the study
☐	☒ Antibodies
☐	☒ Eukaryotic cell lines
☒	☐ Palaeontology and archaeology
☐	☒ Animals and other organisms
☒	☐ Human research participants
☒	☐ Clinical data
☒	☐ Dual use research of concern

Methods

n/a	Involved in the study
☒	☐ ChIP-seq
☒	☐ Flow cytometry
☒	☐ MRI-based neuroimaging

Antibodies

Antibodies used	mouse monoclonal TOM20 (BD Biosciences #612278, 1:1000), TOMM20 (Abcam #ab186734, 1:200), cGAS (CST #15102, 1:100), TFAM (Proteintech #22586-1-AP, 1:500), TFAM (Abcam #ab119684, 1:1000), DNA (Millipore #CBL186, 1:200), HSP60 (CST #12165, 1:1000), HSP60 (EnCor Biotechnology #CPCA-HSP60, 1:1000), Twinkle (Abcam #ab83329, 1:100), POLG2 (Proteintech #10997-2-AP, 1:100), mtSSB (Proteintech #12212-1-AP, 1:100), RAB7 (CST #9367, 1:100), Activated BAX (Santa Cruz Biotechnology #sc-23959, 1:100), TOP3A (Proteintech #14525-1-AP, 1:500), DRP1 (BD Biosciences #611113, 1:1000), PARP (CST #9542, 1:1000), VDAC1 (Abcam #ab15895, 1:1000), HRP-conjugate β-Actin (clone 13E5, CST #5125, 1:1000), Peroxidase (HRP) Anti-Rabbit IgG Goat Secondary Antibody (CST #7074P2, 1:2000), Peroxidase (HRP) Anti-Mouse IgG Horse Secondary Antibody (CST #7076P2, 1:2000), Goat Anti-Chicken IgY H&L (Alexa Fluor® 405) (Abcam #ab175674, 1:250), Donkey anti-Mouse IgG (Alexa Fluor™ 488) (Invitrogen #A21202, 1:500), Donkey anti-Mouse IgG (Alexa Fluor™ 568) (Invitrogen #A10037, 1:500), Goat anti-Rabbit IgG (Alexa Fluor™ 488) (Invitrogen #A11008, 1:500), Donkey anti-Mouse IgG (Alexa Fluor™ 568) (Invitrogen #A10037, 1:500), Goat anti-Rabbit IgG (Alexa Fluor 750) (Invitrogen #A-21039, 1:250)
Validation	mtSSB (Proteintech #12212-1-AP): validated by western blot (band at predicted molecular weight) and immunofluorescence (predicted localization) by manufacturer. https://www.ptglab.com/products/SSBP1-Antibody-12212-1-AP.htm mouse monoclonal TOM20 clone 29 (BD Biosciences #612278): validated by western blot (band at predicted molecular weight) and immunofluorescence (predicted localization) by manufacturer. https://www.bdbiosciences.com/en-us/products/reagents/microscopy-imaging-reagents/immunofluorescence-reagents/purified-mouse-anti-tom20.612278 TOMM20 clone EPR15581-39, Abcam #ab186734): validated by western blot (band at predicted molecular weight) and immunofluorescence (predicted localization) by the manufacturer. https://www.abcam.com/tomm20-antibody-epr15581-39-mitochondrial-marker-ab186734.html

cGAS clone D1D3G, (CST #15102): validated by western blot (band at predicted molecular weight) by the manufacturer. https://www.cellsignal.com/products/primary-antibodies/cgas-d1d3g-rabbit-mab/15102

TFAM (Proteintech #22586-1-AP): validated by western blot (band at predicted molecular weight) by the manufacturer, and by us using TFAM-deficient cells to show a reduction in the band corresponding to TFAM (see Extended Data Figure 2). https://www.ptglab.com/products/TFAM-Antibody-22586-1-AP.htm

TFAM clone 18G102B2E11 (Abcam #ab119684): validated by western blot by the manufacturer (band at predicted molecular weight), and by us for immunofluorescence using conditions known to deplete TFAM (see Extended Data Figure 1 and West et al., Nature, 2015). https://www.abcam.com/mttfa-antibody-18g102b2e11-mitochondrial-marker-ab119684.html

DNA clone clone AC-30-10, (Millipore #CBL186): validated by immunofluorescence by us, as used in our previous publication (West et al., Nature, 2015). https://www.sigmaaldrich.com/US/en/product/mm/cbl186?gclid=Cj0KCQiAm4WsBhCiARIsAEJIEzWTGAq6NFYATfspWn0biImtfkhASPYXvrfM2BmfnJtvAvEeSUJjHVkaAi4DEALw_wcB

RAB7 clone D95F2 (CST #9367): validated by western blot (band at predicted molecular weight) and immunofluorescence (predicted localization) by the manufacturer. https://www.cellsignal.com/products/primary-antibodies/rab7-d95f2-xp-rabbit-mab/9367

Activated BAX clone B-9 (Santa Cruz Biotechnology #sc-23959): validated by western blot (band at predicted molecular weight) by the manufacturer, and used in previous publications (Riley et al., 2018). https://www.scbt.com/p/bax-antibody-b-9?gad_source=1&gclid=Cj0KCQiAm4WsBhCiARIsAEJIEzWQz9moHFQA_gdLiRSk0k-68B3qpdclCdZzdg2HXlwIBm9EFkJ12AMaAm2GEALw_wcB

HSP60 clone D6F1, (CST #12165, 1:1000): validated by western blot (band at predicted molecular weight) and immunofluorescence (predicted localization) by manufacturer. https://www.cellsignal.com/products/primary-antibodies/hsp60-d6f1-xp-rabbit-mab/12165

HSP60 (EnCor Biotechnology #CPCA-HSP60): validated by western blot (band at predicted molecular weight) and immunofluorescence by manufacturer. https://encorbio.com/product/cpca-hsp60/

POLG2 (Proteintech #10997-2-AP): validated by western blot (band at predicted molecular weight) and immunofluorescence (predicted localization) by manufacturer. https://www.ptglab.com/products/POLG2-Antibody-10997-2-AP.htm

Twinkle (Abcam #ab83329): validated by western blot (band at predicted molecular weight) by manufacturer. https://www.abcam.com/twinkle-antibody-ab83329.html

TOP3A (Proteintech #14525-1-AP, 1:500): validated by western blot (band at predicted molecular weight) by manufacturer. https://www.ptglab.com/products/TOP3A-Antibody-14525-1-AP.htm

DRP1 (clone 8), (BD Biosciences #611113): validated by western blot (band at predicted molecular weight) by manufacturer. https://www.bdbiosciences.com/en-us/products/reagents/microscopy-imaging-reagents/immunofluorescence-reagents/purified-mouse-anti-dlp1.611113

PARP (CST #9542): validated by western blot by manufacturer (band at predicted molecular weight). https://www.cellsignal.com/products/primary-antibodies/parp-antibody/9542

VDAC1 (Abcam #ab15895): validated by western blot by manufacturer (band at predicted molecular weight). https://www.abcam.com/products/primary-antibodies/vdac1porin-antibody-mitochondrial-loading-control-ab15895.html

Eukaryotic cell lines

Policy information about cell lines

Cell line source(s)	IMR-90 and U2OS cells were obtained from the ATCC. CRISPR-knockout U2OS pools were obtained from Synthego. Lenti-X HEK293T cells were obtained from TakaRa Clonetech.
Authentication	IMR-90 and U2OS cells were authenticated by ATCC (STR profiling for both). CRISPR-knockout pooled cells were authenticated by western blotting and sequencing. No information about authentication of Lenti-X HEK293T was found on the manufacturer website.
Mycoplasma contamination	Cells lines were tested monthly for mycoplasma and confirmed negative.
Commonly misidentified lines (See ICLAC register)	No commonly misidentified cell lines were used.

Animals and other organisms

Policy information about studies involving animals; ARRIVE guidelines recommended for reporting animal research

Laboratory animals	Tfam+/- mice are in the C57BL/6 background. 2-12 month old female mice were used to make mouse embryonic fibroblasts (MEFs). All housing and experiments were done using IACUC-approved protocols in AAALAC-certified facilities with the following details below. Temperature- Animal holding rooms are equipped with NIST Traceable™ Fischer Scientific temperature and humidity recorders. T/H min/max readings are monitored and recorded daily on an electronic APP by ARD technicians. Acceptable temperature ranges for rodents are 70º (+/- 2Fº).The system is designed to trigger email alerts to Supervisors, Managers and Veterinarians when environmental parameters are outside recommended range for immediate evaluation and response. T/H min/max readings recorded on the APP also feed into a database and generate daily, monthly, and annual reports for each room in the animal facilities. Temperatures are also monitored by Facility Services. Deviations trigger alerts to the watch engineers for appropriate responses. Humidity is not controlled but is monitored daily by computerized sensors or by hygrothermographs. Because supply air is 100% fresh air, humidity in the animal facilities is approximately the same as the outside ambient air (typically 30-70% humidity year-round). All room air is exhausted to the exterior of the building. HVAC- The Facility Services Department performs quarterly pre-filter changes and evaluations and annual main filter change, fan change, and rebalance of HVAC system. Animal holding rooms are maintained between 10-15 air changes per hour and room prefilters are changed monthly (or more often as needed) by ARD personnel. Door seals, door sweeps, and door closures are in place to eliminate drafts. Static-pressure differentials have been established. Criteria are set dependent on animal species, health status, and traffic flow which are monitored by magnahelic gauges or through Johnson Control Systems. Enrichment- All mice are provided Bed'r NestTM (The Andersons) nesting material. Cage grommet (air/valve port on the inside of

cage) provides mice an area to perch. Wire bar feeder provides mice an area to hang, climb and chew.
Lighting- Lighting is provided on a diurnal cycle, generally 6:00 a.m. to 6:00 p.m., with a photoperiod of 12 hours through a time-controlled lighting system.

Wild animals
No wild animals were used.

Field-collected samples
No field-collected samples were used.

Ethics oversight
Salk Institute and Yale University animal care and use committee

Note that full information on the approval of the study protocol must also be provided in the manuscript.